Journal of Molecular Structure 1244 (2021) 130986

Contents lists available at ScienceDirect

Journal of Molecular Structure

journal homepage: www.elsevier.com/locate/molstr

Stabilization of the ruthenium (II) and -(III) centres by chelating N-donor ligands: Synthesis, characterization, biomolecular affinities and computational studies

Sanam Maikoo[a], Irvin Noel Booysen[a,*], Bheki Xulu[a], Lydia Rhyman[b,c], Ponnadurai Ramasami[b,c]

[a] School of Chemistry and Physics, University of KwaZulu-Natal, Pietermaritzburg, South Africa
[b] Computational Chemistry Group, Department of Chemistry, Faculty of Science, University of Mauritius, Réduit 80837, Mauritius
[c] Centre of Natural Product, Department of Chemical Sciences, University of Johannesburg, Doornfontein, Johannesburg 2028, South Africa

ARTICLE INFO

Article history:
Received 20 February 2021
Revised 21 June 2021
Accepted 25 June 2021
Available online 30 June 2021

Keywords:
Ruthenium
Spectral characterization and crystal structures
Computational studies
DNA/BSA interaction studies
Radical scavenging

ABSTRACT

Anticancer activities of ruthenium Schiff base metal complexes have been closely correlated to their steric factors and physicochemical properties. The core objectives of our research study were to synthesize and characterize new ruthenium Schiff base compounds derived from cinnamaldehyde, cuminaldehyde or 4-aminoantipyrine. In addition, the stereo-electronic features of the aforementioned metal compounds and two selected previously reported ruthenium Schiff base compounds were related to their antioxidant and biomolecular interaction capabilities. Therefore, we demonstrated the formation of novel mononuclear ruthenium(III) compounds with chelating N-donor ligands: *fac*-[$RuCl_3(PPh_3)$(ap)] (**1**) (ap = 4-aminoantipyrine), *trans*-P-[$Ru(PPh_3)_2$(cinap)$_2$](PF_6) (**2**) (cinap = 1,5-dimethyl-2-phenyl-4-{[3-phenylprop-2-en-1-ylidene]amino}-1,2-dihydro-3*H*-pyrazol-3-one) and *cis*-Cl, *trans*-P-[$RuCl_2(PPh_3)_2$(cumbh)] (**3**) (cumbh = *N*'-(4-isopropylbenzylidene)benzohydrazide). Structural confirmations were conducted primarily by spectroscopic techniques while the single crystal X-ray analysis revealed the distorted octahedrons of the respective metal compounds. Voltammetry experiments of **1**–**3** illustrated one-electron quasi-reversible redox waves which are attributed to metal oxidation state interconversions. CT-DNA binding affinities and modes of the novel metal complexes **1**–**3** as well as the formerly published ruthenium Schiff base compounds, *trans*-P, *cis*-Cl-[Ru(pch)$Cl_2(PPh_3)_2$] (**4**) (pch = 4-((pyridine-2yl-imino)methylene)-chromone) and *cis*-[$RuCl_2$(bpap)(PPh_3)] (**5**) (bpap = 2,6-*bis*-((antipyrine-imino)methylene)pyridine) were experimentally and computationally investigated. The paramagnetism of **1**–**4** and the proton-donor abilities of all the metal compounds promoted significantly higher NO and DPPH radical scavenging activities than the natural antioxidant, vitamin C. Experimental electronic BSA titrations revealed that the metal compounds are ideal binders which preferentially bind to site **IIA**. The X-ray and spectroscopic data were supported by the computed data which was simulated using the density functional theory method.

1. Introduction

Innovative metal-based anticancer drugs are essential to evolve their current chemotherapeutic efficacies from the current lack of specificity and prevalent cancer resistant development of established platinum-based drugs. In particular, ruthenium shares similar electronic and redox properties to its physiologically-relevant group congener, iron and these commonalities have accounted to lower toxicity to non-cancerous cells of the ruthenium-anticancer compounds than platinum chemotherapeutic drugs. In addition, non-sterically hindered ruthenium anticancer drugs can be regarded as pro-drugs as their substitution kinetics towards biological nucleophiles and bimolecular modes of interactions mimics that of cisplatin [1].

However, the next generation of ruthenium anticancer drugs should have tailored biodistribution patterns and hence current design strategies entail the inclusion of bio-active moieties into multidentate ligands, that can facilitate bioavailability, target-specificity and cytotoxicity. This design strategy is illustrated in the diamagnetic arene ruthenium(II) compound, Ru(η^5-Cp)(PPh_3)(2,2'-bipy-4,4'-R)]$^+$ (*R* = dibiotin ester) which contains biotinylated

* Corresponding author.
E-mail address: Booyseni@ukzn.ac.za (I.N. Booysen).

https://doi.org/10.1016/j.molstruc.2021.130986
0022-2860/

groups anchored *via* a bipyridine chelator [2]. The aforementioned metal complex salt showed markedly higher anticancer activities than cisplatin in selected breast cancer cell lines. The use of Schiff bases not only allow the stabilization of ruthenium in its common oxidation states +II or +III but also inclusion of various bio-vectors within different Schiff base architectures [3]. In our present research study, we have utilized chromone-, antipyrine-encompassing imines and cinnamaldehyde, cuminaldehyde-derived Schiff bases as potential biomarkers for cancerous cells.

The secondary metabolite, chromone has been incorporated as a pharmacophore in various medicinal drugs while those derived from the essential oils, cinnamaldehyde and cuminaldehyde portrays a wide variety of their inherent antioxidant and antimicrobial activities as well as new bio-activities [4,5]. Particularly, Schiff bases of the essential oils when coordinated to M(II) centers afforded metallo-drugs, [Ni(tcum)$_2$] (Htcum = cuminaldehyde thiosemicarbazone) and [Cu(tcin)(H$_2$O)Cl] (Htcin = *trans*-cinnamaldehyde thiosemicarbazone), which exhibited proliferation against the U937 human cell lines [6]. Organic derivatives of antipyrine have also displayed a broad range of anticancer activities which has been improved for ruthenium complexes containing antipyrine analogous [7]. Ruthenium Schiff base complexes with chromone and antipyrine groups have also shown considerable biological activities, namely [Ru(η^6-*p*-cymene)-(chromone)Cl] and [RuCl(CO)(PPh$_3$)L] (HL = 4-(2-(2-hydroxyphenyl)ethylideneamino)-1,2-dihydro-2,3-dimethyl-1-phenylpyrazol-5-one) produced good cytotoxic effects when screen against the human cervical cancer cell line, HeLa [8,9].

Probing the interactions between metal complexes and various biomolecules are essential in elucidating plausible mechanisms of anticancer activity [10–12]. In particular, Schiff base ruthenium compounds have illustrated distinctive binding to DNA nucleic acids and protein residues in enzymes associated cancer pathogenesis and their uptake by human serum album is critical for effective physiological distribution [13–15]. Imino ruthenium compounds can also infer antioxidant activities by scavenging reactive oxygen species (ROS) which have been correlated with DNA mutation [15,16]. A typical example includes the octahedral ruthenium(III) species: [RuCl(AsPh$_3$)L^1] (H$_2$L^1 = *bis*-(salicylaldehyde)-*S*-methylisothiosemicarbazone) and [RuCl(AsPh$_3$)L^2] (H$_2$L^2 = *bis*-(5-chloro-salicylaldehyde)-*S*-methylisothiosemicarbazone) which could intercalate between the DNA base pairs despite the presence of the bulky AsPh$_3$ co-ligand within their respective coordination spheres [17]. Furthermore, the individual unpaired *d*-electrons of the paramagnetic metal complexes rendered superior radical neutralizing capabilities over vitamin C and butylated hydroxytoluene. In addition, the ruthenium compounds could form adducts with BSA where quenching rate (K_q) constants ranging in the vicinity of 10^5 M^{-1} were attained.

In this research study, three novel ruthenium(III) compounds were isolated from equimolar reactions of the metal precursor, *trans*-[RuCl$_2$(PPh$_3$)$_3$] precursor with each of the Schiff bases, cumap (1,5-dimethyl-2-phenyl-4-[4-(propan-2-yl)benzylidene]amino-1,2-dihydro-3*H*-pyrazol-3-one) cinap (1,5-dimethyl-2-phenyl-4-[3-phenylprop-2-en-1-ylidene]amino-1,2-dihydro-3*H*-pyrazol-3-one) and *N*'-(4-isopropylbenzylidene)benzohydrazide (cumbh). These coordination reactions resulted in the formation of the paramagnetic metal compounds *fac*-[RuCl$_3$(PPh$_3$)(ap)] (**1**), *trans*-P-[Ru(PPh$_3$)$_2$(cinap)$_2$] (**2**) and *cis*-Cl, *trans*-P-[RuCl$_2$(PPh$_3$)$_2$(cumbh)] (**3**). Structural elucidations were established using single X-Ray diffraction and supplemented with spectroscopic characterization. Interestingly for **1**, the solid state structure showed that cumap underwent hydrolysis and consequently, only the ap moiety coordinated to the *trans*-[RuCl$_2$(PPh$_3$)$_3$] unit, as opposed to **2** and **3** where the Schiff bases remained intact upon coordination. Furthermore, the antioxidant abilities and biological interactive studies with DNA and BSA of the above mentioned compounds, as well as two previously synthesised compounds containing the chromone and 4-aminoantipyrine moieties (*trans*-P, *cis*-Cl-[Ru^{III}(pch)Cl$_2$(PPh$_3$)$_2$] (**4**) (pch = 4-((pyridine-2ylimino)methylene)-chromone) and *cis*-[Ru^{II}Cl$_2$(bpap)(PPh$_3$)] (**5**) (bpap = 2,6-*bis*-((antipyrine-imino)methylene)pyridine)) were investigated [18]. In addition, we used density functional theory method to complement the experimental studies.

2. Experimental

2.1. Materials and methods

The metal precursor, *trans*-[RuCl$_2$(PPh$_3$)$_3$] as well as the organic precursors, 4-aminoantipyrine, cinnamaldehyde, cuminaldehyde, benzohydrazide and ammonium hexafluorophosphate were all acquired from Sigma-Aldrich. High purity ascorbic acid, Sodium nitroprusside, 2,2-diphenyl-1-picrylhydrazyl (DPPH), Griess reagent, phosphate buffered saline tablets (PBS), calf thymus (CT)-DNA, bovine serum albumin (BSA), Ibuprofen, Warfarin and electrochemical analysis grade and tetrabutylammonium hexafluorophosphate were also procured from Sigma Aldrich. Organic solvents were purchased from Merck SA and used without further purification. The Schiff bases, cumap and cinap, as well as the ruthenium(II) metal compounds **4** and **5** were prepared according to literature methods [18,19].

^{1}H NMR spectra were run in the solvent d^6-DMSO by using a Bruker Advance 400 MHz spectrometer equipped with an autosampler. A Bruker EMX-Plus X-band spectrometer operated at 9.83 GHz was used for EPR measurements at room temperature. Operation parameters were as follows: microwave power of 2 mW, centre magnetic field of 330 mT, sweep width of 200 mT, modulation frequency of 100 kHz and modulation amplitude of 0.6 mT. Electronic spectra were run on a Perkin-Elmer Lambda 25 whereas solid-state infrared spectra were collected on a Perkin-Elmer Spectrum 100. Melting point ranges were attained with a Stuart SMP3 melting point device. Redox properties of the respective ruthenium compounds were explored using a Metrohm Autolab potentiostat combined with a three electrode system: a glassy carbon working electrode (GCWE), a pseudo Ag|AgCl reference electrode and an auxiliary Pt counter electrode. Electrochemical grade tetrabutylammonium hexafluorophosphate (0.1 M) was utilized as a supporting electrolyte to the 2 mM dichloromethane solutions of the metal compounds. Fluorescence experiments were conducted using a 1 cm quartz emission cell and a Perkin Elmer LS-45 fluorescence spectrometer with a xenon lamp source.

2.2. Synthesis of N'-(4-isopropylbenzylidene)benzohydrazide (cumbh)

The compound cumbh was formed from the condensation reaction between benzohydrazide (0.250 g, 1.84 mmol) and cuminaldehyde (0.272 g, 1.84 mmol) in the presence of three drops of glacial acetic acid, see **Scheme 1**. The reaction mixture was heated until reflux in ethanol (30 cm^3) for 5 h. A light-yellow solution was attained which was cooled to room temperature and then filtered. Excess cuminaldehyde was removed by washing with petroleum ether to afford a cream precipitate. Yield: 61 %; m.p: 192.1–196.0 °C. IR (ν_{max}/cm^{-1}): υ(N-H)$_{amide}$ 3236; υ(C=O)$_{ketonic}$ 1647; υ(C=N)$_{imine}$ 1551. ^{1}H NMR (295 K/ d^6 - CD$_6$SO/ ppm, see **Fig. S1**): 8.45 (s, 1H, *H10*); 7.92 (d, 2H, *H6, H8*); 7.69–7.51 (m, 6H, *N2H, H13, H14, H15, H16, H17*); 7.36 (d, 2H, *H5, H9*); 2.95 (*p*, 1H, *H2*); 1.244 (d, 6H, *H1, H1', H1", H3, H3', H3"*). UV-Vis (DCM, ε, M^{-1} cm^{-1}): 229 nm (10100); 306 nm (17540).

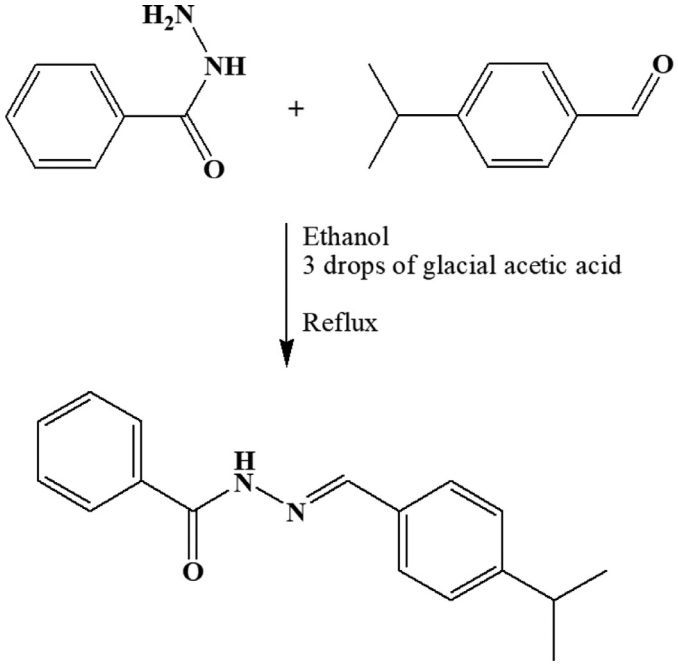

Scheme 1. The condensation reaction between benzohydrazide and cuminaldehyde.

2.3. Synthesis of $[RuCl_3(PPh_3)(ap)]$ (**1**)

A 1:1 molar reaction between cumap (0.0348 g, 0.104 mmol) and *trans*-$[RuCl_2(PPh_3)_3]$ (0.100 g, 0.104 mmol) was carried out at elevated temperature until reflux for 5 hours in toluene (30 cm^3). The dark red solution was cooled to room temperature, filtered at stored at STP conditions. After several days, rectangular-shaped, red crystals were formed in the mother liquor which were appropriate for X-ray analysis. Yield: 46 %. m.p: 271.6–274 ºC. IR (ν_{max}/cm^{-1}): υ(N-H) 3050 (m); υ(C=O) 1565 (s); υ(Ru-[PPh_3]) 692 (vs). UV-Vis (DCM, ε, M^{-1} cm^{-1}): 290 nm (20540); 339 nm (18310); 461 nm (3360). Anal. Found: C, 60.653; H, 4.065; N, 5.225. Anal. Calcd. (with 2 molecules of toluene): C, 60.32; H, 5.06; N, 4.91.

2.4. Synthesis of trans-P-$[Ru(PPh_3)_2(cinap)_2](PF_6)$ (**2**)

A mixture of cinap (0.0331 g, 0.104 mmol), *trans*-$[RuCl_2(PPh_3)_3]$ (0.100 g, 0.104 mmol) and ammonium hexafluorophosphate (17.00 mg, 0.104 mmol) in methanol (20 cm^3) was heated until reflux for 3 h. The green solution was then cooled to room temperature and filtered. Yield: 32 %. m.p: 216.4–220.0 ºC. IR (ν_{max}/cm^{-1}): $\upsilon(C{=}N)_{imine}$ 1486 (s); $\upsilon(N\text{-}C\text{-}O)_{enolic}$ 1184 (m); υ(Ru-[PPh_3]$_2$) 693, 746 (vs). UV-Vis (DCM, ε, M^{-1} cm^{-1}): 359 nm (19480); 418 nm (sh, 9590); 629 nm (2470). Crystals for elemental analysis were grown from the slow diffusion of hexane into a chloroform solution of **2**. Anal. Found: C, 57.198; H, 3.789; N, 5.186. Anal. Calcd. (with 1 molecule of PF_6^- and 2 molecules of chloroform): C, 56.91; H, 4.41; N, 5.11.

2.5. Synthesis of cis-Cl, trans-P-$[RuCl_2(PPh_3)_2(cumbh)]$ (**3**)

Equimolar amount of cumbh (0.0278 g, 0.104 mmol) and *trans*-$[RuCl_2(PPh_3)_3]$ (0.100 g, 0.104 mmol) were heated until reflux in ethanol (20 cm^3) for 4 hours. The resulting green solution was cooled to room temperature and filtered. Green rectangular crystals formed from the slow diffusion methods using a DCM: hexane solvent system. Yield: 27%. m.p: 259.5–265.0 ºC. IR (ν_{max}/cm^{-1}): $\upsilon(C{=}N)_{imine}$ 1479 (s); $\upsilon(N\text{-}C\text{-}O)_{enolic}$ 1186 (m); υ(Ru-[PPh_3]$_2$) 689, 742 (vs). UV-Vis (DCM, ε, M^{-1} cm^{-1}): 260 nm (sh, 18360); 265 nm (sh, 17870); 271 nm (sh, 14330); 325 nm (5420); 389 nm (sh, 3260); 624 nm (1200). Anal. Found: C, 60.479; H, 4.150; N, 2.727. Anal. Calcd (with 1 molecule of DCM): C, 59.98; H, 4.47; N, 2.59.

2.6. X-Ray diffraction

Crystallographic data for the mononuclear compounds was collected on a Bruker Apex Duo furnished with an Oxford Instruments Cryojet. The diffractometer was operated at a low temperature of 100(2) K and an Incoatec microsource was tuned at 30 W power. Their crystal and structure refinement are summarized in **Table 1** while the experimental geometrical parameters are shown in **Tables 2–4**. An X-ray beam was generated with MoKα radiation source with a wavelength of 0.71073 Å and radiation exposures were at a common crystal-to-detector distance of approximately 50 mm. In addition, data collection was achieved *via* omega and phi scans at 0.50º frame widths, using APEX2 [20]. Data reduction were implemented with the aid of the SAINT program [20], whereby scan speed scaling, standard Lorentz and polarization correction factors and also outlier rejection were applied. A semi-empirical multi-scan absorption correction algorithm, SADABS was used for data correction [21]. Direct methods, WinGX [22] and SHELX-2016 [23] were applied to the solid-state structures. The *x, y, z* coordinates of the non-hydrogen atoms were established using the difference density map and anisotropically refined with SHELX-2016 [23]. Furthermore, three-dimensional orientations of the hydrogens were incorporated as idealized contributors in the least squares process and their positions were computed using a standard riding model with $C\text{-}H_{methylene}$ distances of 0.99 Å, U_{iso} = 1.2 U_{eq}, $C\text{-}H_{methyl}$ distances of 0.98 Å, U_{iso} = 1.5 U_{eq}, $C\text{-}H_{aromatic}$ distances of 0.93 Å and U_{iso} = 1.2 U_{eq}.

2.7. Computational studies

Density functional theory (DFT) method was used to perform all computations. Full geometry optimisations using the X-ray structures of complexes **1**-**3** were carried out using the B3LYP [24,25] functional in the gas phase with the LANL2DZ (Los Alamos National Laboratory 2 double-ζ) [26–28] basis set on all atoms. The LANL2DZ effective core potential (ECP) basis set on the ruthenium atom, the 6-31G(2d,p) basis for chlorine atom and the 6–31G(d,p) basis for carbon, nitrogen, phosphorus and oxygen atoms and 6-31G basis for hydrogen atom were also used and this basis set combination is denoted as BS1. In addition, the def2-tzvp basis set for ruthenium atom and cc-pVDZ basis set for all other atoms were also employed and this is denoted as BS2. The selected combination of B3LYP and basis sets provide reliable results as previously justified in the literature [29,30]. Frequency computation of each of the optimised geometry was also performed to ensure that the complex was a true local minimum.

Full optimisations of complexes **1-3** were performed using the CAM-B3LYP [31] functional in conjunction with the BS1 and BS2 basis sets in dichloromethane (DCM) using the polarisable continuum model (PCM). This was followed by TD-DFT computations to simulate the electronic spectra and to have a better understanding of the electronic transitions. Transition energies and oscillator strengths for the electronic excitation of the first 70 excited states of each complex were considered.

All the computations were carried out at 298.15 K and 1 atm. Gaussian 09 [32] was used for the optimisation using the B3LYP/LANL2DZ method in the gas phase only for which the relatively low Root-Mean-Square-Deviation (RMSD) values between the optimized conformer and the solid-state structures were generated, see **Fig. S2**. All the other computations were performed using Gaussian16 [33].

Table 1
Crystal data and structure refinement data for metal compounds 1 - 3.

Compound	**1**• C_7H_8	**2**•2(PF_6)	**3**
Chemical formula	$C_{29}H_{28}Cl_3N_3OPRu$• C_7H_8	$C_{76}H_{68}N_6O_2P_2Ru$•	$C_{53}H_{47}Cl_2N_2OP_2Ru$
Formula weight	765.07	1550.31	961.83
Temperature (K)	100(2)	100(2)	100(2)
Crystal system	Monoclinic	Monoclinic	Monoclinic
Space group	$P2_1/c$	$P2_1/n$	$P2_1/c$
Unit cell dimensions (Å, º)	a = 17.1746(14)	a = 13.8422(13)	a = 22.6852(19)
	b = 10.2679 (9)	b = 14.9830(12)	b = 10.6935(9)
	c = 19.9184(15)	c = 16.8327(15)	c = 20.1473(15)
	α = 90	α = 90	α = 90
	β = 103.950(3)	β = 104.312(4)	β = 109.933 (3)°
	γ = 90	γ = 90	γ = 90
Crystal size (mm)	0.31 × 0.18 × 0.12	0.21 × 0.14 × 0.09	0.24 × 0.19 × 0.11
V (Å^3)	3409.0(5)	3382.7(5)	4594.6 (6)
Z	4	2	4
Density (calc.) (Mg/ m^3)	1.491	1.522	1.390
Absorption coefficient (mm^{-1})	0.78	0.41	0.57
F (000)	1564	1588	1980
Θ range for data collection (deg)	2.7°; 26.3°	2.5°; 26.5°	2.7°; 28.3°
Index ranges	-21 ≤ h ≤ 20	-16 ≤ h ≤ 17	-30 ≤ h ≤ 30
	-8 ≤ k ≤ 12	-18 ≤ k ≤ 13	-14 ≤ k ≤ 14
	-23 ≤ l ≤ 24	-21 ≤ l ≤ 20	-26 ≤ l ≤ 22
Reflections measured	21296	24263	44634
Observed reflections ($I > 2\sigma$ (I)	6965	6825	11302
Independent reflections	5034	4729	9305
Data/ restraints/ parameters	6965/ 2/ 406	6825/ 0/ 459	11302 / 0/ 522
Goodness of fit on F^2	1.02	1.10	1.01
Observed R; wR^2	0.043; 0.091	0.072; 0.150	0.034; 0.077
R_{int}	0.053	0.044	0.046

Table 2
Selected bond lengths [Å] and angles [º] for complex 1.

	Experimental	B3LYP/LANL2DZ	B3LYP/BS1	B3LYP/BS2
Ru-Cl1	2.355(1)	2.397	2.399	2.385
Ru-Cl2	2.318(1)	2.436	2.340	2.331
Ru-Cl3	2.342(1)	2.432	2.393	2.380
Ru-P	2.304(1)	2.614	2.367	2.353
Ru-O	2.101(2)	2.296	2.200	2.180
Ru-N3	2.201(3)	1.910	2.243	2.223
N2-N3	1.401(4)	1.432	1.411	1.410
C1-O	1.274(4)	1.276	1.254	1.255
C2-N3	1.438(4)	1.371	1.428	1.429
C1-N1	1.374(4)	1.385	1.378	1.379
C3-N2	1.366(5)	1.392	1.390	1.391
O-Ru-N3	83.3(1)	80.3	81.4	81.8
P-Ru-Cl2	90.26(4)	88.3	93.2	93.3
Cl1-Ru-Cl3	169.42(4)	161.6	165.7	166.1
P-Ru-N3	178.61(8)	172.1	176.9	177.3
O-Ru-Cl2	173.20(7)	167.4	170.8	170.7

Table 3
Selected bond lengths [Å] and angles [º] for complex 2.

	Experimental	B3LYP/LANL2DZ	B3LYP/BS1	B3LYP/BS2
Ru-O1	2.153(3)	2.196	2.197	2.179
Ru-O2	2.153(3)	2.196	2.197	2.179
Ru-N1	2.112(4)	2.137	2.158	2.134
Ru-N2	2.112(4)	2.137	2.158	2.134
Ru-P1	2.4066(14)	2.592	2.505	2.484
Ru-P2	2.4065(14)	2.592	2.505	2.484
C9-N1	1.276(7)	1.366	1.334	1.338
C26-N4	1.276(7)	1.366	1.334	1.338
N2-N3	1.390(7)	1.439	1.411	1.408
N5-N6	1.390(7)	1.439	1.411	1.408
N2-C11	1.352(7)	1.438	1.405	1.405
N3-C13	1.359(7)	1.378	1.363	1.364
N5-C28	1.352(7)	1.378	1.405	1.405
N5-C30	1.359(7)	1.438	1.475	1.474
C30-O2	1.275(6)	1.298	1.268	1.269
C13-O1	1.275(6)	1.298	1.268	1.269
P1-Ru-P2	180	180.0	180.0	180.0
O1-Ru-O2	180	180.0	180.0	180.0
N1-Ru-N4	180	180.0	180.0	180.0
N1-Ru-O1	82.63(14)	80.6	80.2	80.6
N4-Ru-O2	82.63(14)	80.6	80.2	80.6
N1-Ru-O2	97.37(14)	99.4	99.8	99.4
N4-Ru-O1	97.37(14)	99.4	99.8	99.4

2.8. UV-Vis spectrophotometric DNA titrations

The CT-DNA interactive studies of **1** - **3** were done at a pH of 7.2 in phosphate-buffered saline (PBS). The CT-DNA solution in PBS produced a ratio of 1.9:1 at 260 nm and 280 nm, which proposes that the CT-DNA was effectively free of protein. The molar absorption coefficient (ε_{260} = 6600 M^{-1} cm^{-1}) was used in calculating the CT-DNA concentration per nucleotide [34]. The resulting CT-DNA stock solution was kept at 4 ºC and used within a 48 h window. Solutions of the metal complexes and CT-DNA were incubated at 25 ºC for 24 h preceding any UV-Vis measurements [35]. Afterwards, UV-Vis spectra of standard solutions for the individual metal compounds were collected in methanol and observed after the addition of varying concentrations of CT-DNA in PBS buffer. The intrinsic binding constant (K_b) was determined by fitting the titration data into the following equation:

$$\frac{[DNA]}{(\varepsilon_a - - \varepsilon_f)} = \frac{[DNA]}{(\varepsilon_b - - \varepsilon_f)} + \frac{1}{K_b(\varepsilon_b - - \varepsilon_f)} \quad (A)$$

In the overhead equation, [DNA] is equivalent to the concentration of DNA in base pairs, ε_a matches the extinction coefficient of the particular absorption band at the specified DNA concentration (corresponding to A_{obs}/[complex]), ε_f corresponds to the extinction coefficient of the free compound in solution, and ε_b is equated to the extinction coefficient of the fully bound compound to DNA. The plot of [DNA]/[ε_a - ε_f] versus [DNA], produces a slope of 1/[ε_a - ε_f] and a Y intercept of 1/K_b[ε_b - ε_f]. The ratio of the slope to the intercept is expected to be the intrinsic binding constant (K_b) [35].

Table 4
Selected bond lengths [Å] and angles [º] for complex 3.

	Experimental	B3LYP/LANL2DZ	B3LYP/BS1	B3LYP/BS2
Ru-Cl1	2.3449(7)	2.420	2.386	2.374
Ru-Cl2	2.3360(6)	2.447	2.383	2.370
Ru-O	2.029(2)	2.054	2.077	2.058
Ru-N1	2.065(2)	2.121	2.148	2.125
Ru-P1	2.39365(5)	2.487	2.503	2.484
Ru-P2	2.4074(6)	2.487	2.482	2.463
C10-N1	1.289(3)	1.305	1.302	1.306
N1-N2	1.404(2)	1.440	1.376	1.378
C11-N2	1.314(3)	1.326	1.317	1.319
C11-O2	1.281(2)	1.321	1.296	1.297
O1-Ru-N1	76.33(6)	75.9	74.5	75.0
Cl1-Ru-Cl2	99.67(2)	99.1	100.4	99.9
P1-Ru-P2	176.51(2)	176.0	175.7	175.2

2.9. Antioxidant studies

The experimental method for the radical scavenging experiments were modified from literature methods [36,37]. Each experiment was carried out in triplicate to safeguard data reproducibility. The standard equation (B) was employed to find the experimental percentage radical scavenging activities:

$$\%\ Radical\ scavenging\ activity = \left(\frac{A_c - A_f}{A_c}\right) x\ 100 \qquad (B)$$

where A_c is the control's absorbance (NO or DPPH radicals) and A_f is the absorbance following the addition of the different metal compounds to the control. The IC_{50} values (concentrations which induce 50% radical scavenging activity) of the metal compounds were calculated from their distinctive experimental percentage radical scavenging activities. The experiment for the DPPH radical assay was performed by running the control's UV-Vis spectrum [DPPH (0.2 mM in MeOH)] followed by the addition of 1 cm^3 of a solution of metal compound [30 μM in MeOH] and thereafter the sample solution was shaken to guarantee homogeneity. Then, the sample solution underwent incubation in the dark for 20 min and its UV-Vis spectrum was run.

The following experimental technique was used for the NO radical assay: initially, a 10 mM solution of sodium nitroprusside was made up in PBS buffer and incubated for 3 h at room temperature. Subsequently, 1 cm^3 of Griess reagent was added to a 0.5 cm^3 of the nitroprusside solution and this resulting solution functioned as the control. The UV-Vis spectrum of the control was run. The sample solutions were prepared by the adding each metal compound (30 μM in MeOH) to a 0.5 cm^3 aliquot of sodium nitroprusside. After 3 h of incubation, 1 cm^3 of Griess reagent was added to each sample solution and their respective UV-Vis spectra were run.

2.10. BSA binding interaction studies

The BSA stock concentration was determined spectrophotometrically by means of an extinction coefficient of 43824 M^{-1} cm^{-1} (at 280 nm) and using a solution prepared in PBS buffer at a pH of 7.2 [38]. The sample solutions of **1**–**5** were prepared in MeOH.

2.10.1. Electronic spectrophotometric titrations

The BSA interaction experiments were carried out by keeping the BSA concentration constant (~20 µM) whilst varying the concentrations of the individual metal compounds (0-~320 µM). A 2 min incubation was used for the sample mixtures. Equivalent volumes of metal compound were added to both the sample and reference cells. The titration data was fitted to the following equation:

$$\left[\frac{A_o}{A_o - A}\right] = \left(\frac{\varepsilon_{BSA}}{\varepsilon_B}\right) + \left(\frac{\varepsilon_{BSA}}{\varepsilon_B\ .K_{app}}\right).\left(\frac{1}{C_{compound}}\right) \qquad (C)$$

where A_0 and A are equivalent to the absorbances of BSA at 280 nm in the absence and presence of a metal compound, ε_{BSA} and ε_B are the extinction coefficients of BSA and the bound complex (*viz.* adduct of a metal complex and BSA), K_{app} is equal to the apparent association constant and $C_{compound}$ is the concentration of a metal complex. The following double reciprocal plot can be produced from the equation (**C**) and the apparent association constant (K_{app}) is determined from the ratio of the intercept to the slope [39].

$$\frac{1}{(A_o - A)}\ vs\ \left(\frac{1}{C_{complex}}\right)$$

2.10.2. Fluorescence emission spectroscopic titrations

The effects on the emission spectrum of BSA upon increasing the metal compounds' concentrations were evaluated. Fluorescence emission spectra were performed at 293 K with the width of excitation and emission slits adjusted to 5 nm. The spectra were run within a wavelength range of 300–500 nm at an excitation of 280 nm. The data was used to estimate the Stern-Volmer quenching constant (K_{SV}) by means of the Stern-Volmer relationship [40]:

$$\frac{I_0}{I} = 1 + K_{SV}\ [complex] \qquad (D)$$

where I_0 and I are emission intensities in the absence and presence of each metal compound. The K_{SV} values were determined from the slope of:

$$\frac{I_0}{I}\ vs\ [complex] \qquad (E)$$

The quenching rate constant (K_q) could then be calculated from equation (**F**):

$$K_{SV} = K_q\ \tau_0 \qquad (F)$$

where τ_0 is the lifetime of the protein (10^{-8} s) without a quencher.

2.10.3. Competitive binding studies

Competitive binding experiments were carried out by employing two site markers (competitors), *viz*., warfarin for site I and ibuprofen for site II. First, an equivalent concentration of the competitor was added to BSA (each at 5 µM) and variations in the fluorescence spectra were observed. The fluorescence titration was then achieved by varying the concentration of each metal compound in the BSA-competitor solution and noting the spectral changes [41]. The titration data was also fitted to the Stern-Volmer plot (equation **E**) and the attained quenching and rate constants were compared to the values in the absence of the competitors [42].

3. Results and discussion

3.1. Synthesis, spectral characterization and redox properties of complexes 1-3

Equimolar coordination reactions of the respective Schiff bases: cumap, cinap and cumbh with *trans*-$[RuCl_2(PPh_3)_2]$ afforded the paramagnetic complexes, $[RuCl_3(PPh_3)ap$ (**1**), *trans*-P-$[Ru(PPh_3)_2(cinap)_2]$ (**2**) and *cis*-Cl, *trans*-P-$[RuCl_2(PPh_3)_2(cumbh)]$ (**3**) which were isolated in low to moderate yields, see **Scheme 2**. It is clearly evident from the spectroscopic data of **1** that the cumap Schiff base hydrolyzed upon coordination which afforded the neutral bidentate $N_{amino}O_{ketonic}$ coordination mode of the ap (4-aminoantipyrine) moiety whilst the cinap and cumbh Schiff bases remained intact in their corresponding metal compounds, **2** and **3**, see **Figs. 1 - 3**. The cinap ligand (for **2**) coordinated in a '2 + 2' manner through its monoanionic donor sets ($N_{imine}O_{enol}$) while

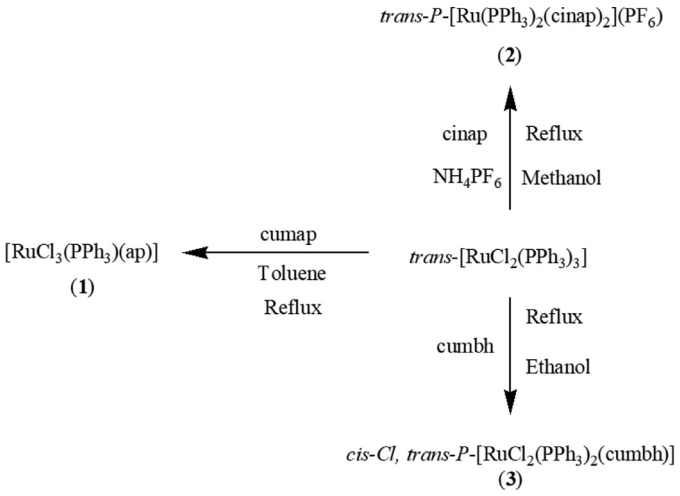

Scheme 2. Synthetic routes for the paramagnetic ruthenium complexes 1 – 3.

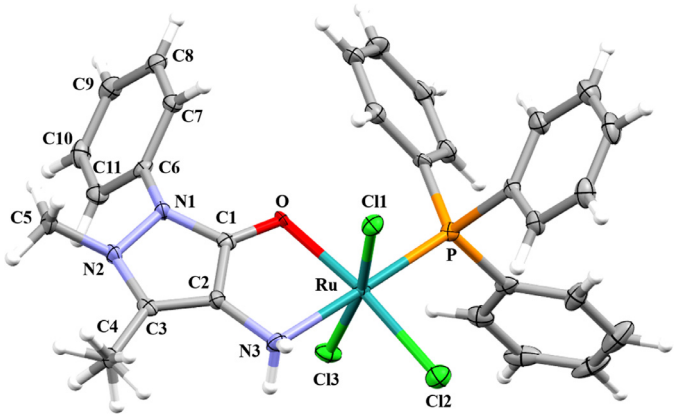

Fig. 1. ORTEP view of metal complex 1 showing 50 % probability displacement ellipsoids and the atom labelling. The solvent molecule of recrystallization has been omitted for the sake of clarity.

the remaining octahedral coordination sites are occupied by triphenylphosphine co-ligands, see **Fig. 2**. In contrast to **2**, only a single unit of the cumbh ligand functioned as a monoanionic chelator ($N_{imine}O_{enol}$) for **3** leading to the stabilization of the paramagnetic metal centre by the *cis*-orientated chloride and *trans*-positioned triphenylphosphonine co-ligands, see **Fig. 3**. In our recent study, we have computationally illustrated that the Schiff base functionality of cumap is weaker compared to that of cinap [19]. Consequently, the latter rationalized the formation of **1** and **2**. The hydrolysis of cumap is caused by water which originates from the open atmosphere and then diffuses into the reaction mixture.

In addition, the monomeric metal complexes display also mid to high solubility in polar aprotic solvents and moderate solubility in alcoholic media. The experimental and simulated IR spectra of complexes **1-3** are displayed in **Figs. S3** – **S8**. In general, both the B3LYP/BS1 and B3LYP/BS2 methods are in agreement with each other. The IR spectrum of **1** show medium-to-strong bands ascribed to the vibrations of the amino and ketonic bonds while an intense vibrational band at 692 cm^{-1} is ascribed to (Ru-[PPh_3]) [43]. Computed wavenumbers for the Ru-P stretching are found at 537 cm^{-1}. The most characteristic peak is assigned to stretching vibrations of C-O and C=C in the region of 1680 cm^{-1} while the C-N stretching corresponds to the intense peak in the region of

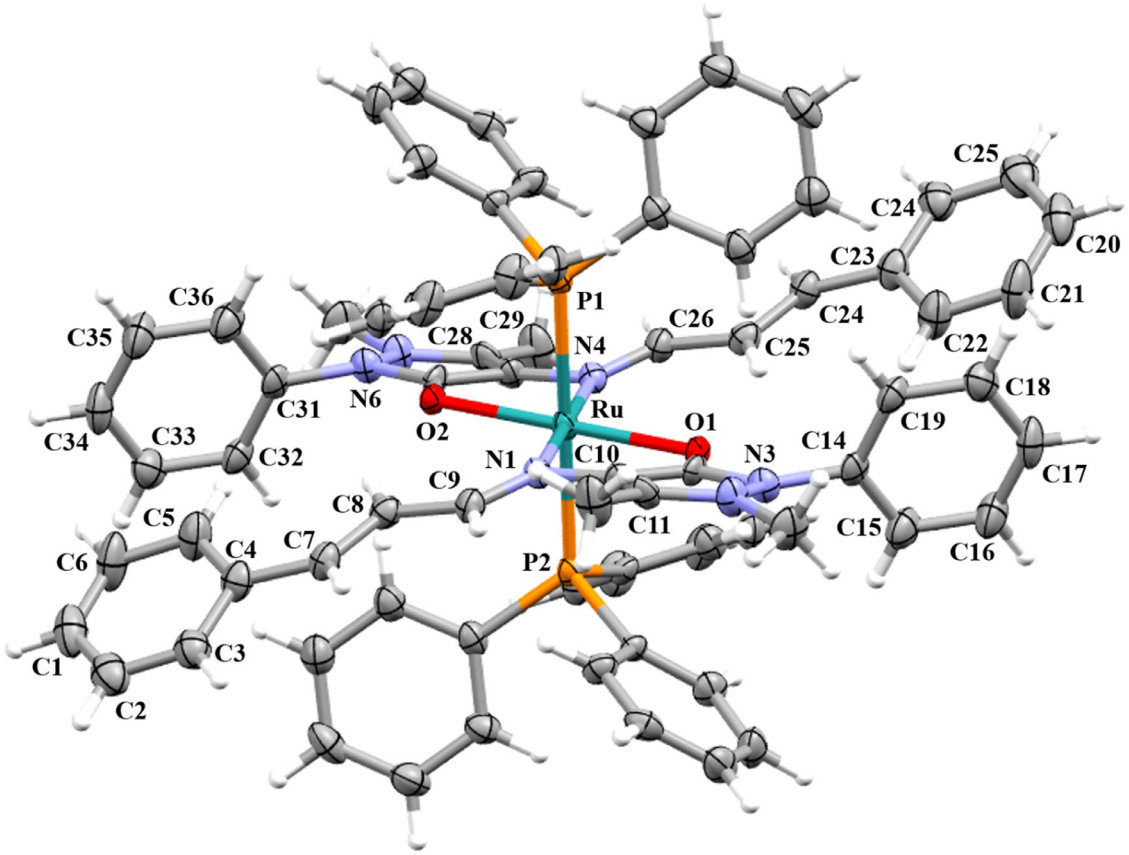

Fig. 2. ORTEP view of compound 2 showing 50 % probability displacement ellipsoids and the atom labelling. The counterion has been omitted.

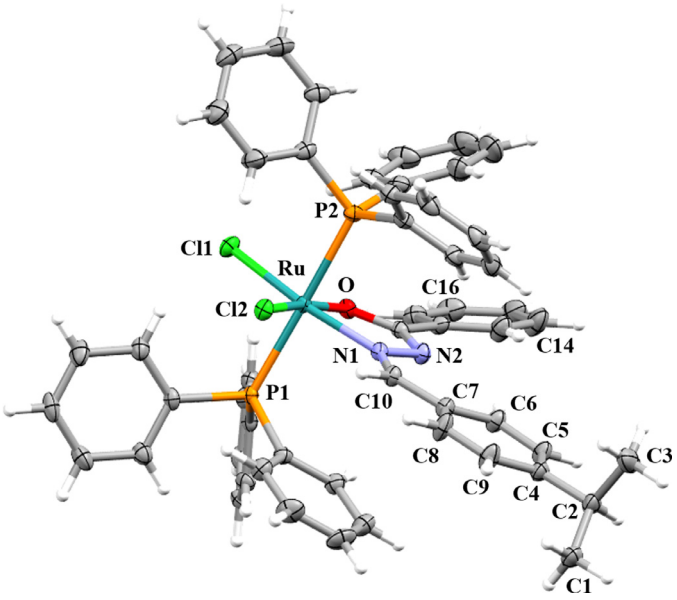

Fig. 3. ORTEP view of metal complex 3 showing 50 % probability displacement ellipsoids and the atom labelling.

1317 cm^{-1}. The actual *trans*-[$Ru(PPh_3)_2$] of **2** and **3** unit appears dual finger print bands between 689–746 cm^{-1}.

The hydrolysis of the cumap is confirmed by the absence of its imino signal (at 1595 cm^{-1}) in the IR spectrum of **1** while a shift of the ketonic vibrational band to a lower frequency, is suggestive of coordinative bonding between the ketonic oxygen and the metal center. Furthermore, shifts are also observed when comparing the IR spectra of **2** and **3** with their corresponding free-ligands' IR spectra whereby the $\nu(C{=}N)_{imino}$ signals occur at lower frequencies in those of the metal complexes than those of their related free-ligands. In the IR spectrum of **2**, the signals associated with the ketonic C=O bond (originally observed at 1637 cm^{-1} in the IR spectrum of the free-ligand) disappears which is a distinctive feature of the enol form of the chelator coordinating [44].

The most intense peak computed in the region of 1500 cm^{-1} of complex **2** is assigned to the stretching of the C=C bond of the alkene group while the peaks observed in the region of 1200 cm^{-1} corresponds to the stretching of the C-N bond. The overlay IR spectra of **3** and its uncoordinated ligand, indicates the loss of the N-H amide group which is represented by the disappearance of the infrared stretch at 3236 cm^{-1} and a new infrared stretch (appearing at 1186 cm^{-1}) emanating from the formation of the C-O enolic signal. Hence, the latter IR spectral changes support the conversion of cumbh to its enol form, and its subsequent deprotonation upon coordination to the metal centre [45, 46]. The experimental C-O stretching frequency is in agreement with the computed wavenumbers at 1183 cm^{-1}. Computationally, the most intense peak in the region of 1550 cm^{-1} in the simulated IR spectra of complex **3** corresponds to C=N stretching band.

The uncorrected computed wavenumbers of the complexes **1 - 3** allowed the assignments of the stretching vibrations related to the Ru metal centres and these are listed in **Table S1**. The computed wavenumbers are in agreement with experimental IR absorptions reported in literature; the Ru-Cl stretching vibrations are reported within the range of 320–220 cm^{-1} [47,48] and the Ru-N stretching vibrations are observed in the range of 650–250 cm^{-1} [49]. The Ru-O and Ru-P stretching vibrations have been experimentally observed within the range of 520–450 cm^{-1} [50,51] and around 555 cm^{-1} [50], respectively.

Electronic spectra of **1** – **3** display several absorption bands in the UV region below 400 nm, which are readily assigned to ligand-centred $\pi - \pi^*$ and $n - \pi^*$ transitions occurring within the Schiff base chelates [51, 52], see **Figs. S9 – S11**. Broad absorption bands appearing in the visible region in the spectra of **1** and **2**, between 418–461 nm, are mainly attributed to Ligand-to-Metal Charge Transfer (LMCT) bands. Truncated intensity $d - d$ transitions are observed for **2** and **3** at 629 and 624 nm respectively, due to their low-spin d^5 electronic configurations. However, no metal-based electronic transition was observed for **1** which hints at the ap moiety acting as a strong-field ligand that culminates into a larger crystal-field splitting energy [53].

The computed electronic spectra of **1 - 3** are displayed in **Figs. S12 - S14** which allowed for the interpretation of detailed electronic transitions within the complexes, refer to **Tables S2 – S10**. Since the Ru has an unpaired electron in the complexes, the singly occupied molecular orbitals (SOMOs) result into α and β orbitals. The simulated UV-Vis spectrum of complex **1** is illustrated in **Fig. S12** indicating two absorption peaks at 234 and 387 nm using the CAM-B3LYP/BS1 method. The main orbital transitions at 234 nm are S-2(α)→L+2(α) (21%) and S-3(β)→L+3(β) (29%). The first orbital transition illustrates a charge transfer from the Ru metal's *d* orbitals and *p* orbitals of Cl atoms to the cumap chelator; while the second orbital transition is accounted to electron density redistribution of the cumap ligand and *p* orbitals of Cl atoms to the *d* orbitals of the Ru metal. In addition, a secondary orbital electronic transition of S-2(β)→L+2(β) (19%) mainly concerns the *d* orbitals on Ru atom and delocalisation of electron density within the PPh_3 moiety. The peak at 387 nm corresponds to two primary electronic transitions, S-8(β)→L(β) (44%) and S-3(β)→L(β) (109%), which have LMCT character, particularly from the cumap to the *d* orbitals of the Ru atom. However, an artefact of the CAM-B3LYP/BS1 method is observed for the orbital contribution of 109%. Likewise, two absorption peaks at 235 and 348 nm are observed, with the B3LYP/BS2 method, which are of metal-to-ligand charge transfer (MLCT) character when considering both α and β orbitals.

The simulated electronic spectrum of complex **2**, which is illustrated in **Figure S13**, has a peak at 293 nm (CAM-B3LYP/BS1) which mainly arises from the S-7→L in both the α (50%) and β (37%) orbitals. The transition involving the α orbitals corresponds to the LMCT while that involving the β orbitals corresponds to ligand-to-ligand charge transfer. The peak at 430 nm arises due to the S(β)→L(β) (115%) which leads to MLCT character, originating from the d_{z^2} orbitals of the Ru metal to the ligand. Once again, an artefact of the CAM-B3LYP/BS1 method is observed for the orbital contribution of 115%. Two peaks are observed using the CAM-B3LYP/BS2 method at 285 and 374 nm. Both peaks correspond mainly to LMCT.

The simulated UV-Vis spectrum of complex **3** show two major transitions with high oscillator strengths as shown in **Table S8**. The broad absorption band peak observed with the CAM-B3LYP/BS1 method consists of two peaks at 267 and 317 nm. The peak at 267 nm corresponds to the S-1(β)→L+2(β) (51%) transition consisting of the electron transfer within the Ru and Cl atoms while the peak at 317 nm mainly corresponds to S(α)→L(α) (34%) ligand-to-ligand charge transfer. Two distinct transitions at 257 and 325 nm are observed using the CAM-B3LYP/BS2 method. The peak at 257 nm indicates mainly transition within the Ru and Cl atoms along with LMCT character, particularly from cumbh to the Ru atom and the peak at 325 nm consists mainly of the ligand-to-ligand charge transfer.

The paramagnetic nature of the metal centres for the respective metal compounds were determined by ambient ESR spectroscopy, see Fig. 4. Asymmetry within the octahedrons of **1** and **3** is clearly evident which culminates into poor resolved rhombic patterns (g_x = 2.27 for **1** and 2.26 for **3**) [54]. In contrast,

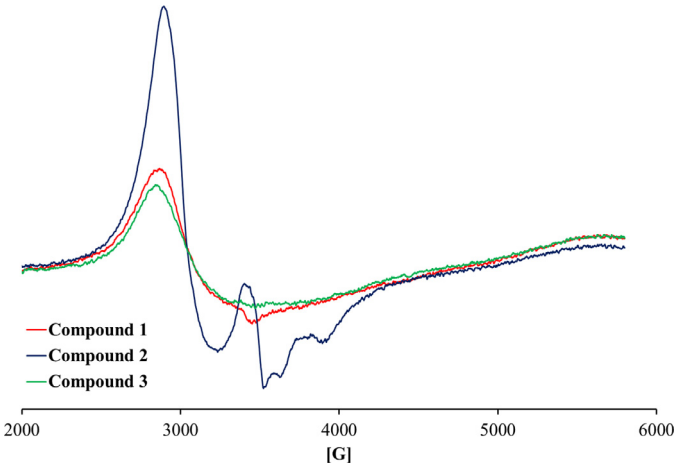

Fig. 4. Overlay solution ESR spectra of the respective metal compounds.

the symmetrical orientation of the co-ligands occupying coordination sphere of **2** renders three signals, *viz.* g_x = 2.42, g_y = 2.00 and g_z = 1.78. Overall, the nature of the ESR spectra and *g*-values obtained are characteristic of octahedral organoruthenium(III) complexes. Typical examples in literature includes the paramagnetic ruthenium compounds *trans*-[RuCl(AsPh$_3$)$_2$(Nap-Nmtsc)] (Nmtsc = napthaldehyde-*N*-methylthiosemicarbazide) and *trans*-[RuCl$_2$(AsPh$_3$)$_2$(L$_2$)] (HL$_2$ = 4-methoxy-2-hydroxybenzophenone) exhibit respective isotropic and rhombic ESR spectra with *g*-values ranging from 1.84 to 2.36 [54, 55].

Electron-transfer properties of **1–3** were probed in dichloromethane *via* cyclic voltammetry (CV) and squarewave voltammetry (SWV), see **Figs. S15 - S17**. The CVs of the metal compounds shows single redox waves which are all considered as quasi-reversible as their peak-to-peak separations differ from the standard ferrocene (ΔE_p = 90 mV *vs* Ag| AgCl), refer to **Table S11**. Notably, sharp peaks are observed within CV of **1** which are typical of adsorption on working electrode surface [56]. The propensity of **1** to induce electrode modification is tentatively ascribed to its smaller size which allows its molecules to immobilize as a thin film on the GCE. The redox couples of **1** ($E_{½}$ = 0 V *vs* Ag | AgCl) and **2** ($E_{½}$ = 1.11 V *vs* Ag | AgCl) can be readily ascribed to respective Ru(II)/Ru(III) and Ru(III)/Ru(IV) couples whereas the redox couple of **3** ($E_{½}$ = -1.05 V *vs* Ag | AgCl) is assigned to the d^5/d^6 interconversions [57–59]. These assignments are based on the similarity of their half-wave potentials with that of other ruthenium(III) species, *e.g. mer*-[Ru^{III}(bpy)(CH$_3$OH)Cl$_3$] (bpy = bipyridine) display redox couples of -0.33 and +1.32 V (*vs* Ag| Ag$^+$) [57–59].

3.2. Crystallographic description

The mononuclear compounds **2** and **3** both exhibit a monoclinic crystal system with **2** co-crystallizing with a PF_6 counter-ion in a $P2_1/n$ space group while **3** crystallizing as a single molecule in a $P2_1/c$ space group, see **Figs. 1 - 3**. Hydrogen-bonded dimers of **1** crystallizes along with toluene molecules of recrystallization, see **Fig. S18**. Non-classical close contacts between the hexafluorophosphate counter-ions and their adjacent molecules of **2** allows these molecules to pack in columns aligned with the [*b*]- and [*c*]-axes. Similarly, non-polar interactions between neighbouring molecules of **3** orientate co-planar with respect to the [*b*] and [*c*]-axes.

Constrained five-membered chelate rings [O-Ru-N3 = 83.3(1)°, O1-Ru-N1/ O$_2$-Ru-N4 = 82.63(14)° and O1-Ru-N1 = 76.33(6)°] within the respective ruthenium compounds induce octahedral distortion. In particular, the opposing donor atoms of **1** affords non-linear bond angles [Cl1-Ru-Cl3 = 169.42(4)°, P-Ru-N3 = 178.61(8)° and 173.20(7)°. Furthermore, the N1-Ru-O1 [82.63(14)°], N4-Ru-O2 [82.63(14)°], N1-Ru-O2 [97.37(14)°] and N4-Ru-O1 [97.37(14)°] bond angles of **2** that constitute the O2N4O1N1 basal plane differ from the idealized value of 90° but the P1-Ru-P2, O1-Ru-O2 and N1-Ru-N4 are linear. Contrastingly, the *trans*-[Ru(PPh$_3$)$_2$]$^{3+}$ [176.51(2)°] of **3** is non-linear and it has a wide Cl1-Ru-Cl2 [99.67(2)°] bond angle.

As expected, the Ru-O$_{ketonic}$ bond of **1** [2.101(2) Å] is shorter than the Ru-O$_{enol}$ bond of **2** [Ru-O1/O2 = 2.153(3) Å] but the latter is longer Ru-O$_{enol}$ bond of **3** [2.029(2) Å] which is due to variable *trans*-influence imposed on the by their respective enolic O-donor atoms. Though, the analogous bonds [1.984(1) and 2.003(1) Å] of the paramagnetic ruthenium compound, [RuCl(obs)$_2$(PPh$_3$)$_2$] (Hobs = 2-hydroxyphenylbenzothiazole) were comparable to those of **3** [60]. Indicatively, the hybridization of the nitrogen donor atoms can be discriminated based on the respective Ru-N$_{amino}$ [2.201(3) Å for **1**] and Ru-N$_{imino}$ [2.112(4) Å for **2** and 2.201(3) Å for **3**] bond lengths. As per literature trend, the higher Lewis acidic character of **2** and **3** affords elongated ruthenium-to-nitrogen bonds than the '3+3' ruthenium(II) Schiff base complex, [Ru(tpsal)$_2$] (Htpsal = 3,5-*di-tert*-butyl-*N*-(2-(methylsulfanyl)phenyl)-salicylaldimine) with Ru-N$_{imino}$ bond distances of 2.051(5) and 2.053(5) Å. However, the Ru^{III}-N$_{amino}$ bonds are especially rare where predominately shorter Ru^{II}-N$_{amino}$ bonds of monomeric diamagnetic ruthenium complexes were found in the Cambridge Crystallographic Database Centre (CCDC) [61–63]. *Trans-axial* orientations of the triphenylphosphine co-ligands in **2** [Ru-P1 = 2.4066(14) Å and Ru-P2 = 2.4065(14) Å] and **3** [Ru-P1 = 2.39365(5) Å and Ru-P2 = 2.4074(6) Å] affords similar Ru-P bonds whereas in **1** [Ru-P = 2.304(1) Å], the amino nitrogen imposes on a stronger trans-effect on the phosphorus donor atom. These ruthenium-to-phosphorous distances and the chloro-coordination [Ru-Cl1 = 2.355(1) Å, Ru-Cl2 = 2.318(1) Å for **1** and Ru-Cl1 – 2.3449(7) Å, Ru-Cl2 = 2.3360(6) Å for **2**] bonds are comparable to other ruthenium(III) complexes found within literature [64–67].

The comparison between the ketonic bond of **1** [C1-O = 1.274(4) Å] and the enol bonds of the other metal compounds [C30-O2 = 1.275(6) Å for **2** and C30-O2 = 1.281(2) Å for **3**] unequivocally show that the former exhibit double bond character. Indicatively, the C1-N1 [1.374(4) Å], C2-N3 [1.438(4) Å], C3-N2 [1.366(5) Å] single bonds of **1** are elongated when compared to the imino bonds of **2** [C9-N1/ C26-N4 = 1.276(7) Å] and **3** [C10-N1 = 1.374(4) Å]. Interestingly, the characteristic N-N intracyclic antipyrine bonds of **1** [N2-N3 = 1.401(4) Å] and **2** [N2-N2/ N5-N6 = 1.390(7) Å] compares well with the corresponding aliphatic bond of **3** [N1-N2 = 1.404(2) Å]. Consequently, the neighbouring C11-N2 [C11-N2 = 1.314(3) Å] bond is a localized *pi*-bond whereas those of the C-N antipyrine moieties of **1** and **2** [N2-C11/ N5-C28 = 1.352(7) Å and N3-C13/ N5-C30 = 1.359(7) Å] are sigma bonds. The computed structural parameters of complexes **1–3** are comparable to those determined by the X-ray diffraction although they are slightly larger than the experimental values, refer to **Tables 2 - 4** [68]. The root mean square deviations (RMSDs) for the bond lengths and bond angles between the computed and experimental structures were also calculated for non-hydrogen atoms (**Table S12**) and the RMSDs indicate that the optimised geometries using both computational methods are in agreement with the experiment.

3.3. Antioxidant studies

Regulation of reactive oxygen species (ROS) within biological media is of utmost importance since normal cellular operation is dependent on the latter [69]. An increase in ROS can cause oxida-

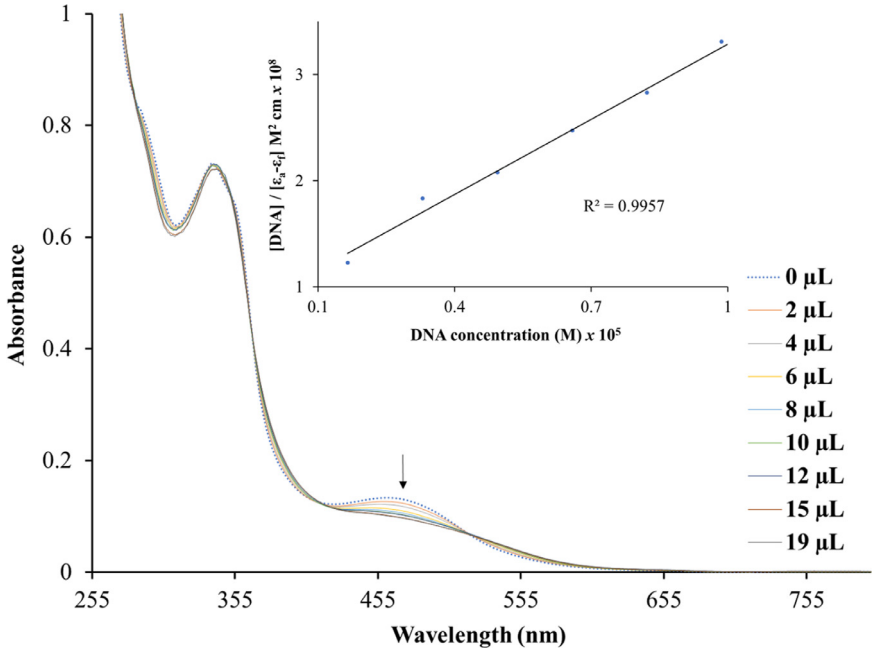

Fig. 5. Overlay UV-Vis spectra of compound 1 in the absence and presence of increasing amounts of CT-DNA. A dashed line indicates the initial spectrum. **Inset**: Plot of [DNA]/(ε_a - ε_f) x 10^8 vs [DNA] $\times$ 10^5 and the linear fit for the titration.

Table 5
Antioxidant activities of 1 – 5 and Vitamin C against the DPPH and NO radicals.

Compound	DPPH Radical IC_{50} (µM)	NO Radical IC_{50} (µM)
1	30	44
2	48	45
3	12	21
4	42	28
5	61	54
Vitamin C	141	210

tive damage to vital biomolecules or tissue which may contribute to numerous diseases, such as, cancer, hypertension and Parkinson's disease [70,71]. Antioxidants derivatized from metal coordination have recently gained attention in safeguarding biological systems from the negative effects of ROS and the Schiff base complexes of ruthenium are among these [53]. The radical scavenging capabilities of **1**–**5** were assessed against the DPPH and NO radicals and compared to the natural antioxidant, Vitamin C (the standard), refer to Table 5. The formulated ruthenium compounds are seen to possess higher DPPH (IC_{50} = 12–61 µM) and NO (IC_{50} = 21–54 µM) radical scavenging activities than the standard (Vitamin C) and are within range if the activities seen for other ruthenium compounds [71,72].

3.4. DNA interaction studies

DNA is a critical target for anticancer transition metal complexes and thus their modes of interactions and affinities towards the CT-DNA is of high importance. Electronic spectroscopy is a technique that is universally employed to assess the binding interactions between metal compounds and DNA. Generally, this is achieved by monitoring changes in the UV-Vis spectral profile of a metal compound when exposed to standardized volumes of Calf Thymus DNA (CT-DNA). Electrostatic or non-intercalative modes of binding may result in a hyperchromic- or hypochromic effects with no significant wavelength shifts. However, an intercalative mode of binding results in a hyperchromic effect with a significant red shift owing to the robust π – π^* stacking interaction between the aromatic chromophore of a chelator and the base pairs of DNA [12,73].

Absorbance spectra of the metal compounds were distinctively changed upon the progressive additions of CT-DNA, see Figs. 5, 6, **S19** – **S21**. Numerous clear isosbestic points are noted in the individual electronic spectral profiles of **1** - **5** which reveal the presence of more than one spectroscopically distinct chromophore in solution (*viz.* free and bound) and is suggestive of a single binding mode of the respective metal complexes with DNA [74]. With the introduction of CT-DNA, hypochromicity along with a slight red shift of the absorption band at 461 nm is detected. Despite the fact that the intrinsic binding constant (K_b) of **1**, 2.67 $\times$ 10^6 M^{-1}, is of the same magnitude as known traditional intercalators (10^6 M^{-1}) [75, 76], it is anticipated that **1** is a DNA groove-binder. This is largely due to the presence of the bulky triphenylphosphine co-ligand which impedes the DNA intercalation of **1**.

Diminishing metal-based electronic transitions for **2** (at 620 nm) and **3** (at 625 nm) accompanied with no batchochromic shifts suggest coordinative bonding between the respective metal compounds and the phosphate group on the backbone or with the DNA base pairs within the major or minor grooves of DNA [77–79]. In addition, an appearance of a charge transfer band at 425 nm in the electronic spectra of **2** is indicative of a new specie forming in solution due to the binding of the metal complex to DNA. A similar trend is seen by a disappearance of an absorption band at 317 nm with a simultaneous appearance of a shoulder at 382 nm in the overlay electronic spectra of **3**. Hypochromism was also observed in the electronic spectral profile of **5** at 383 nm; whilst that of **4** indicates overall hyperchromism.

The intrinsic binding constants (K_b) were found to be between 2.75–7.00 $\times$ 10^5 M^{-1} for **2**–**5**, which further corroborates the fact that their DNA binding mode is indeed non-intercalative since the K_b values are smaller than for known intercalators or partial intercalators like ethidium bromide (1.80 $\times$ 10^6 M^{-1}) or $[Ru(phen)_2(dppz)]^{2+}$ (> 10^6 M^{-1}), which is most likely due to the steric hindrance of the bulky PPh_3 co-ligands [74, 80]. Furthermore, groove-binding ruthe-

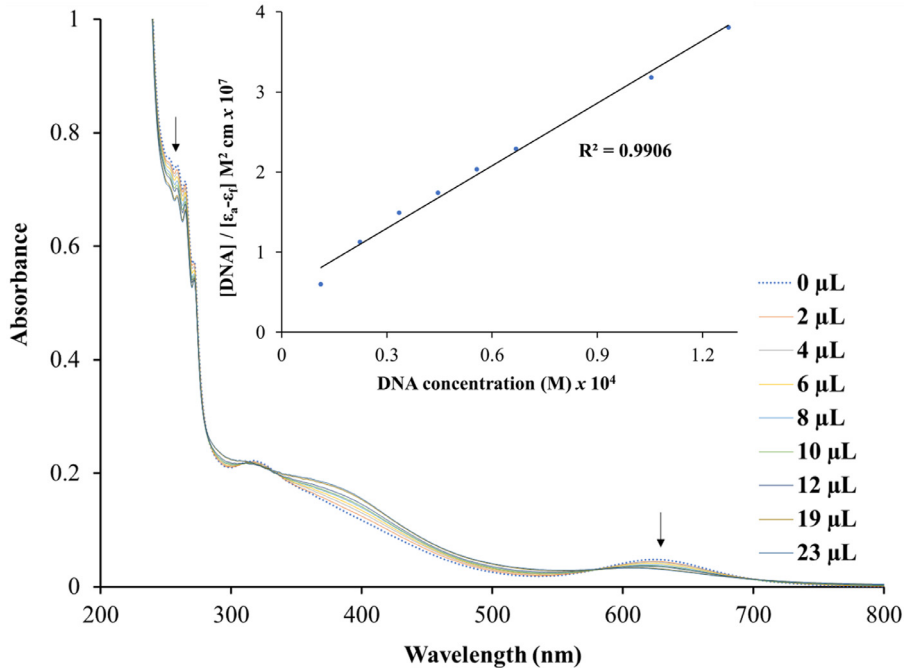

Fig. 6. Overlay UV-Vis spectra of compound 3 in the absence and presence of increasing amounts of CT-DNA. A dashed line indicates the initial spectrum. **Inset**: Plot of $[DNA]/(\varepsilon_a - \varepsilon_f) \times 10^7$ vs $[DNA] \times 10^4$ and the linear fit for the titration.

nium complexes $[Ru(dmp)_2PMIP]^{2+}$ (dmp = 2,9-dimethyl-1,10-phenanthroline and PMIP = 2-(4-methylphenyl)imidazo[4,5-*f*]1,10-phenanthroline) and $[Ru(SPF)(PPh_3)_2Cl_2]$ (SPF = sparfloxacin) have alike K_b values of 2.70×10^5 M^{-1} and 8.41×10^6 M^{-1}, respectively [81,82]. Furthermore, molecular docking simulations illustrated that **2** and **3** dock within the major groove while **1, 4** and **5** docks in close proximity of the B-DNA minor groove, see **Figs. S22 – S26**.

3.5. BSA interaction studies

Serum albumins play important roles in metabolism and have the ability to reversibly bind and hence transport many endo- and exogenous substances in the mammalian system. Consequently, the binding properties of serum albumin with organometal species are often conducted to study the mechanism of interaction between them, which helps contribute to the development of physiologically compatible agents. Bovine serum albumin (BSA) is widely used as the selected protein model due to its structural similarity with human serum albumin (HSA) [83]. In order to evaluate the ability of BSA to function as an appropriate transporter of the selected complexes, the extent of folding (or unfolding) of the BSA strand upon binding with each of the metal compounds was studied by means of UV-Vis and fluorescence spectroscopy. The distinct peaks in the spectra of the protein are due to tryptophan residues within a BSA hydrophobic pocket and therefore, any changes in the spectra reflects conformational changes of the BSA strand. Preferably, the protein should be able retain its native state (folded) as much as possible in order to function as an ideal transporter [84].

Analysing the UV-Vis spectra of BSA, in the presence of incrementing concentrations of **1** – **5**, decreases in the absorbance intensities are observed which indicates that interactions between BSA and the respective metal compounds occurred, see **Figs. S27 - S31** [35,36]. Moreover, slight blue shifts are seen in the absorption maxima in the electronic spectral profiles of **1, 2, 3** and **5** which are characteristic of increased polarity around the tryptophan residue in BSA. Consequently, these metal compounds promote folding of the protein and stabilizing it upon binding by concealing it within the BSA's hydrophobic pocket [85–88]. Contrarily, a red shift was observed in the UV BSA titration profile of **4** which is suggestive of slight unwinding of the BSA strand by the metal complex which exposes the tryptophan residue to a more hydrophilic environment in aqueous media [89, 90].

The apparent association constants (K_{app}) were calculated graphically from the double reciprocal plots of $1/(A_0 - A)$ Versus $1/C_{complex}$ and are shown in **Table S14**. The metal compounds are considered as "ideal" binders towards BSA since their association constants are within range of 10^4 – 10^6 M^{-1} of other strong ruthenium-based binders, with **1, 2**, and **5** having higher binding affinities towards BSA [91–93]. The fluorescence quenching of BSA was investigated in the presence of increasing amount of each metal compound, see **Figs. S32 – S36**. A decrease in the fluorescence intensities of BSA is noticed upon the addition of the respective organometal compounds which is indicative of an interaction between latter and former. Moreover, blue shifts of the emission maxima are seen for **1, 2, 3** and **5**, whilst a red shift is observed for **4**. This validates the UV-Vis study as it suggests that **1, 2, 3** and **5** promotes folding of the BSA strand due to Van der Waals or hydrogen interactions (*i.e.* tryptophan residues moved more into hydrophobic pocket) whilst **4** promotes slight unwinding (*i.e.* tryptophan group moved towards the hydrophilic surface) [94,95]

The Stern-Volmer quenching constants (K_{SV}) and quenching rate constants (K_q) were obtained from the linear Stern-Volmer plots, refer to **Table 6**. The K_{SV} values may be used to assess the binding affinities of the metal compounds towards BSA and the results are consistent with the findings in the UV-Vis study, in that **1, 2** and **5** have higher affinities for BSA. A static quenching mechanism for the ruthenium compounds was confirmed by considerable changes in spectra of the UV-Vis study as well as the fact that the K_q values found are greater than the maximum scatter collision constant responsible for dynamic quenching (2×10^{10} M^{-1} s^{-1}) [91, 94].

BSA shows distinct binding sites with various specificities, the most significant ones being referred to as sites **I** and **II** which are located in hydrophobic subdomains **IIA** and **IIIA**, respectively.

Table 6
Binding parameters of 1 – 5 from BSA fluorescence experiments.

Compound	No Site marker		Ibuprofen		Warfarin	
	K_{SV} (M^{-1})	K_q (M^{-1} s^{-1})	K_{SV} (M^{-1})	K_q (M^{-1} s^{-1})	K_{SV} (M^{-1})	K_q (M^{-1} s^{-1})
1	1.06×10^5	1.06×10^{13}	1.57×10^5	1.57×10^{13}	4.28×10^4	4.28×10^{12}
2	2.12×10^5	2.12×10^{13}	2.11×10^5	2.11×10^{13}	4.42×10^4	4.42×10^{12}
3	5.59×10^4	5.59×10^{12}	3.16×10^4	3.16×10^{12}	2.79×10^3	2.79×10^{11}
4	3.11×10^4	3.11×10^{12}	5.92×10^4	$5.92 \times \cdot 10^{12}$	3.21×10^3	$3.21 \times \cdot 10^{11}$
5	3.38×10^5	3.38×10^{13}	1.26×10^5	1.26×10^{13}	9.38×10^4	9.38×10^{12}

Competitive binding experiments were conducted by observing the fluorescence quenching capabilities of BSA of each metal compound in the presence of a site marker in order to ascertain their preferred binding site within the BSA structure. Site markers are small molecules that have precise binding locations within the BSA structure [96]. In particular, Warfarin was used as a site marker for site **I** whilst Ibuprofen was used for site **II**. As the concentration of each metal compound was increased, the emission maxima of BSA were decreased expressively in the presence of both site markers, see **Figs. S37 – S41**. The Stern-Volmer plots were then used to determine the K_{SV} values for the respective BSA-Warfarin and BSA-Ibuprofen systems. The preferred binding sites of each metal compound was determined by their ability to displace each site marker, this was done by comparing the K_{SV} values in the absence and presence of each site marker. It is seen that the K_{SV} values of the BSA-Ibuprofen systems are not significantly different in magnitude relative to the K_{SV} values in the absence of any site markers, however, a pronounced decrease is seen with the K_{SV} values of the BSA-Warfarin systems. These experimental trends propose that the ruthenium compounds are able to displace Warfarin from its binding site in BSA and therefore assume site **I** (situated in subdomain **IIA**) as the preferred binding site [97].

3.6. Structure-activity relationship

Correlations between the intrinsic properties of the metal compounds and their activities could be derived. It is apparent that the unpaired *d*-electrons of the paramagnetic metal compounds **1 – 4** scavenge the NO and DPPH radicals more efficiently than the diamagnetic metal compound **5**, refer to Table 5 [17,98]. In addition, since all the metal compounds contains pharmacophore derivatives (*viz.* chromone, antipyrine, cinnamaldehyde and cuminaldehyde) that are known radical scavengers *via* proton donation, it is evident that these mechanism of antioxidant activity is inherited by the individual organic chelators of the metal compounds [99–104].

Furthermore, structure-activity relationships could also be deduced from the biomolecular interaction activities. CT-DNA titrations monitored by electronic spectrophotometry unequivocally show that the metal compounds are groove binders which are attributed to the presence of their triphenylphosphine co-ligands which impedes the intercalation of these metal compounds between the DNA base pairs [105]. This is also corroborated by molecular docking simulations which show that **1** fit well into the minor groove opposed to the other metal compounds that fits in the minor groove poorly (for **2** and **5**) or occupies the major groove (for **3** and **4**).

An interesting correlation between the steric factors of the metal compounds and their intrinsic binding constants is observed. More specifically, the lower steric demands of **1** affords a higher K_b value (K_b for **1** = 2.67×10^6 M^{-1}) than the other metal compounds. As mentioned before, the other metal compounds have K_b values in the order of 10^5 M^{-1} which implies that relatively stable DNA-metal compound adducts. The reinforcing interactions that affords the stabilization of the metal compound-DNA hybrids could be largely originating from hydrogen-bonding interactions between DNA base pairs or the sugar-phosphate backbone within grooves and the polar functional groups of the respective organic chelators [106].

Based on the K_{app} and K_{SV} values, metal compounds **1, 2** and **5** are seen to have higher binding affinities towards BSA, refer to Table 6. The higher BSA affinities of **2** and **5** are attributed to the larger sizes of the organic chelators, which encourages increased interactions at BSA's hydrophobic surface while the chloride co-ligands of **1** promote hydrogen-bonding interactions within the hydrophilic BSA cavity [107]. On the contrary, metal compound **4** exhibits the weakest binding ability, which are accounted to its fewer hydrogen bonding sites that culminate into a less stable BSA-metal complex adduct and hence, it does not encourage folding of the protein [108, 109].

4. Conclusions

Paramagnetic ruthenium(III) compounds: *fac*-[$RuCl_3(PPh_3)$(ap)] (**1**) (ap = 4-aminoantipyrine), *trans*-P-[$Ru(PPh_3)_2$(cinap)$_2$](PF_6) (**2**) (cinap = 1,5-dimethyl-2-phenyl-4-[3-phenylprop-2-en-1-ylidene]amino-1,2-dihydro-3*H*-pyrazol-3-one) and *cis*-Cl, *trans*-P-[$RuCl_2(PPh_3)_2$(cumbh)] (**3**) (cumbh = *N'*-(4-isopropylbenzylidene)benzohydrazide) were synthesized and characterized by various physicochemical techniques. In addition, we used DFT method to attain molecular insights of some of the experimental findings. Voltammograms of the respective metal compounds showed quasi-reversible redox processes which were attributed to metal-based interconversion. Structure-activity correlations were deduced by comparing the stereoelectronic properties of the metal compounds with their antioxidant properties as well as DNA and BSA binding affinities. The radical scavenging experiments revealed that all the metal compounds displayed better activities than vitamin C where the paramagnetic metal centres of **1**–**4** promotes better efficacies to neutralize the DPPH and NO radicals. The organic chelators of metal compounds **1**–**5** can serve as proton-donors to render antioxidant responses. The UV-Vis spectrophotometric titrations of the metal compounds with CT-DNA show that they are groove-binders and the strength of the interactions are primarily attributed to the steric factors of the metal compounds. Stabilization of the BSA-metal compounds adducts was enforced by different hydrophobic or hydrophilic functional groups of the metal compounds. Fluorescence and UV-Vis spectrophotometric titrations of each metal compounds against BSA revealed that the former as dynamic quenchers with strong binding affinities towards site **I**. The larger sizes of **1, 2** and **5** were shown to promote stronger binding affinities towards the hydrophobic BSA surface, while the chloride co-ligands of **1** induces hydrogen-bonding interactions inside the hydrophilic BSA cavity.

Credit author statement

Dr Sanam Maikoo performed the experimental work under the supervision of Prof Irvin Noel Booysen. Prof Irvin Noel Booysen and

Dr Sanam Maikoo conceptualized the research study and funding was attained by Prof Irvin Noel Booysen. Dr Lydia Naicker and Prof Ponnadurai Ramasami conducted the DFT studies and the interpretation thereof.

Declaration of Competing Interest

The authors declare no conflict of interests.

Acknowledgements

This research was supported by funding from the National Research Foundation of South Africa (NRF) Incentive Funding for Rated Researchers NRF (Research Grant No. 114737) and University of KwaZulu-Natal. The authors are also grateful to the Centre for High Performance Computing (CHPC) for computational resources. The views expressed are those of the authors and should not be attributed to the NRF, or University of KwaZulu-Natal.

Supplementary materials

Supplementary material associated with this article can be found, in the online version, at doi:10.1016/j.molstruc.2021.130986.

References

[1] A.R. Simović, R. Masnikosa, I. Bratsos, E. Alessio, Chemistry and reactivity of ruthenium (II) complexes: DNA/protein binding mode and anticancer activity are related to the complex structure, Coord. Chem. Rev. 398 (2019) 113011.
[2] L. Côrte-Real, B. Karas, P. Gírio, A. Moreno, F. Avecilla, F. Marques, B.T. Buckley, K.R. Cooper, C. Doherty, P. Falson, Unprecedented inhibition of P-gp activity by a novel ruthenium-cyclopentadienyl compound bearing a bipyridine-biotin ligand, Eur. J. Med. Chem. 163 (2019) 853–863.
[3] A.M. Abu-Dief, I.M. Mohamed, A review on versatile applications of transition metal complexes incorporating Schiff bases, Beni-Suef Univ, J. Basic Appl. Sci. 4 (2015) 119–133.
[4] F.A. Al-Bayati, M.J. Mohammed, Isolation, identification, and purification of cinnamaldehyde from Cinnamomum zeylanicum bark oil. An antibacterial study, Pharmaceutical Biology 47 (2009) 61–66.
[5] N. Wongkattiya, P. Sanguansermsri, I.H. Fraser, D. Sanguansermsri, Antibacterial activity of cuminaldehyde on food-borne pathogens, the bioactive component of essential oil from Cuminum cyminum L. collected in Thailand, Eur. J. Med. Chem. (2019) 163, doi:10.1515/jcim-2018-0195.
[6] F. Bisceglie, S. Pinelli, R. Alinovi, M. Goldoni, A. Mutti, A. Camerini, L. Piola, P. Tarasconi, G. Pelosi, Cinnamaldehyde and cuminaldehyde thiosemicarbazones and their copper(II) and nickel(II) complexes: a study to understand their biological activity, J Inorg Biochem 140 (2014) 111–125.
[7] P. Deshmukh, P.K. Soni, A. Kankoriya, A.K. Halve, R. Dixit, 4-Aminoantipyrine: A significant tool for the synthesis of biologically active Schiff bases and metal complexes, Int. J. Pharm. Sci. Rev. Res 34 (2015) 162–170.
[8] G. Raja, R.J. Butcher, C. Jayabalakrishnan, Studies on synthesis, characterization, DNA interaction and cytotoxicity of ruthenium (II) Schiff base complexes, Spectrochimica acta, Part A, Mole. Biomole. Spectros. 94 (2012) 210–215.
[9] I. Yousuf, F. Arjmand, S. Tabassum, M. Ahmad, Design and synthesis of a DNA intercalative half-sandwich organoruthenium(ii)–chromone complex: cytotoxicity evaluation and topoisomerase Iα inhibition assay, New. J. Chem. 43 (2019) 5475–5487.
[10] L. Riccardi, V. Genna, M. De Vivo, Metal–ligand interactions in drug design, Nat. Rev. Chem. 2 (2018) 100–112.
[11] M. Groessl, M. Terenghi, A. Casini, L. Elviri, R. Lobinski, P.J. Dyson, Reactivity of anticancer metallodrugs with serum proteins: new insights from size exclusion chromatography-ICP-MS and ESI-MS, J. Anal. At. Spectrom. 25 (2010) 305–313.
[12] B.J. Pages, D.L. Ang, E.P. Wright, J.R. Aldrich-Wright, Metal complex interactions with DNA, Dalton Trans. 44 (2015) 3505–3526.
[13] G. Puthilibai, S. Vasudhevan, S.John Mary, Synthesis, spectral, electrochemical and DNA binding properties of ruthenium (III) complexes of Schiff bases containing N,O donor atoms, Materials Today: Proceedings 36 (2021) 809–813.
[14] G. Kalaiarasi, S.R.J. Rajkumar, S. Dharani, J.G. Małecki, R. Prabhakaran, An investigation on 3-acetyl-7-methoxy-coumarin Schiff bases and their Ru (II) metallates with potent antiproliferative activity and enhanced LDH and NO release, RSC. Adv. 8 (2018) 1539–1561.
[15] A. İnan, M. İkiz, S.E. Tayhan, S. Bilgin, N. Genç, K. Sayın, G. Ceyhan, M. Köse, A. Dağ, E. İspir, Antiproliferative, antioxidant, computational and electrochemical studies of new azo-containing Schiff base ruthenium(ii) complexes, New. J. Chem. 42 (2018) 2952–2963.
[16] I.S. Harris, G.M. DeNicola, The complex interplay between antioxidants and ROS in cancer, Trends Cell Biol 30 (2020) 440–451.
[17] G. Prakash, R. Manikandan, P. Viswanathamurthi, K. Velmurugan, R. Nandhakumar, Ruthenium(III) S-methylisothiosemicarbazone Schiff base complexes bearing PPh3/AsPh3 coligand: synthesis, structure and biological investigations, including antioxidant, DNA and protein interaction, and in vitro anticancer activities, J. Photochem. Photobiol. B. 138 (2014) 63–74.
[18] I.N. Booysen, S. Maikoo, M.P. Akerman, B. Xulu, Novel ruthenium(II) and (III) compounds with multidentate Schiff base chelates bearing biologically significant moieties, Polyhedron 79 (2014) 250–257.
[19] M.B. Ismail, I.N. Booysen, M.P. Akerman, Coordination susceptibilities of cinnamaldehyde and cuminaldehyde derived Schiff bases towards the fac-[Re(CO)3]+ core: Formation, computational and DNA interaction studies, Inorg. Chim. Acta 477 (2018) 257–269.
[20] Bruker APEX2, SAINT and SADABSBruker AXS Inc. Madison., Wisconsin, USA, 2010.
[21] R.H. Blessing, An empirical correction for absorption anisotropy, Acta Crystallogr A 51 (1995) 33–38 (Pt 1).
[22] L. Farrugia, WinGX and ORTEP for Windows: an update, J. Appl. Crystallogr. 45 (2012) 849–854.
[23] G. Sheldrick, A short history of SHELX, Acta Crystallographica Section A 64 (2008) 112–122.
[24] A.D. Beck, Density-functional thermochemistry. III. The role of exact exchange, J. Chem. Phys 98 (1993) 5648 -6.
[25] C. Lee, W. Yang, R.G. Parr, Development of the Colle-Salvetti correlation-energy formula into a functional of the electron density, Phys. rev. B 37 (1988) 785.
[26] P.J. Hay, W.R. Wadt, Ab initio effective core potentials for molecular calculations. Potentials for the transition metal atoms Sc to Hg, J. Chem. Phys. 82 (1985) 270–283.
[27] W.R. Wadt, P.J. Hay, Ab initio effective core potentials for molecular calculations. Potentials for main group elements Na to Bi, J. Chem. Phys. 82 (1985) 284–298.
[28] P.J. Hay, W.R. Wadt, Ab initio effective core potentials for molecular calculations. Potentials for K to Au including the outermost core orbitals., J. Chem. Phys. 82 (1985) 299–310.
[29] J. Małecki, Half-sandwich ruthenium (II) complexes with N-and N,(N, O)-donor ligands: molecular, electronic structures, and computational study, Struct. Chem. 23 (2012) 461–472.
[30] T. Liu, K. Wu, L. Wang, H. Fan, Y.-G. Zhou, Z. Yu, Assembled multinuclear ruthenium (II)–NNNN complexes: synthesis, catalytic properties, and DFT calculations, Organometallics 39 (2019) 93–104.
[31] T. Yanai, D.P. Tew, N.C. Handy, A new hybrid exchange–correlation functional using the Coulomb-attenuating method (CAM-B3LYP), Chem. Phys. Lett. 393 (2004) 51–57.
[32] Gaussian 09, Revision A.02, M. J. Frisch, G. W. Trucks, H. B. Schlegel, G. E. Scuseria, M. A. Robb, J. R. Cheeseman, G. Scalmani, V. Barone, G. A. Petersson, H. Nakatsuji, X. Li, M. Caricato, A. Marenich, J. Bloino, B. G. Janesko, R. Gomperts, B. Mennucci, H. P. Hratchian, J. V. Ortiz, A. F. Izmaylov, J. L. Sonnenberg, D. Williams-Young, F. Ding, F. Lipparini, F. Egidi, J. Goings, B. Peng, A. Petrone, T. Henderson, D. Ranasinghe, V. G. Zakrzewski, J. Gao, N. Rega, G. Zheng, W. Liang, M. Hada, M. Ehara, K. Toyota, R. Fukuda, J. Hasegawa, M. Ishida, T. Nakajima, Y. Honda, O. Kitao, H. Nakai, T. Vreven, K. Throssell, J. A. Montgomery , Jr., J. E. Peralta, F. Ogliaro, M. Bearpark, J. J. Heyd, E. Brothers, K. N. Kudin, V. N. Staroverov, T. Keith, R. Kobayashi, J. Normand, K. Raghavachari, A. Rendell, J. C. Burant, S. S. Iyengar, J. Tomasi, M. Cossi, J. M. Millam, M. Klene, C. Adamo, R. Cammi, J. W. Ochterski, R. L. Martin, K. Morokuma, O. Farkas, J. B. Foresman, and D. J. Fox, Gaussian, Inc., Wallingford CT, 2016.
[33] Gaussian 16, Revision B.01, M. J. Frisch, G. W. Trucks, H. B. Schlegel, G. E. Scuseria, M. A. Robb, J. R. Cheeseman, G. Scalmani, V. Barone, G. A. Petersson, H. Nakatsuji, X. Li, M. Caricato, A. Marenich, J. Bloino, B. G. Janesko, R. Gomperts, B. Mennucci, H. P. Hratchian, J. V. Ortiz, A. F. Izmaylov, J. L. Sonnenberg, D. Williams-Young, F. Ding, F. Lipparini, F. Egidi, J. Goings, B. Peng, A. Petrone, T. Henderson, D. Ranasinghe, V. G. Zakrzewski, J. Gao, N. Rega, G. Zheng, W. Liang, M. Hada, M. Ehara, K. Toyota, R. Fukuda, J. Hasegawa, M. Ishida, T. Nakajima, Y. Honda, O. Kitao, H. Nakai, T. Vreven, K. Throssell, J. A. Montgomery , Jr., J. E. Peralta, F. Ogliaro, M. Bearpark, J. J. Heyd, E. Brothers, K. N. Kudin, V. N. Staroverov, T. Keith, R. Kobayashi, J. Normand, K. Raghavachari, A. Rendell, J. C. Burant, S. S. Iyengar, J. Tomasi, M. Cossi, J. M. Millam, M. Klene, C. Adamo, R. Cammi, J. W. Ochterski, R. L. Martin, K. Morokuma, O. Farkas, J. B. Foresman, and D. J. Fox, Gaussian, Inc., Wallingford CT, 2016.
[34] M.E. Reichmann, S.A. Rice, C.A. Thomas, P. Doty, A further examination of the molecular weight and size of desoxypentose nucleic acid, J. Amer. Chem. Soc. 76 (1954) 3047–3053.
[35] M. Kaplanis, G. Stamatakis, V.D. Papakonstantinou, M. Paravatou-Petsotas, C.A. Demopoulos, C.A. Mitsopoulou, Re (I) tricarbonyl complex of 1, 10-phenanthroline-5, 6-dione: DNA binding, cytotoxicity, anti-inflammatory and anti-coagulant effects towards platelet activating factor, J. Inorg. Biochem. 135 (2014) 1–9.
[36] P. Krishnamoorthy, P. Sathyadevi, K. Senthilkumar, P.T. Muthiah, R. Ramesh, N. Dharmaraj, Copper(I) hydrazone complexes: Synthesis, structure, DNA binding, radical scavenging and computational studies, Inorg. Chem. Commun. 14 (2011) 1318–1322.
[37] R. Ramachandran, P. Viswanathamurthi, Ruthenium (II) carbonyl complexes containing pyridine carboxamide ligands and PPh3/AsPh3/Py coligands: synthesis, spectral characterization, catalytic and antioxidant studies, Spectrochim. Acta. A 103 (2013) 53–61.

[38] D.H. Atha, U. Manne, W.E. Grizzle, P.D. Wagner, S. Srivastava, V. Reipa, Standards for immunohistochemical imaging: a protein reference device for biomarker quantitation, J. Histochem. Cytochem. 58 (2010) 1005–1014.

[39] W. Zhong, Y. Wang, J.S. Yu, Y. Liang, K. Ni, S. Tu, The interaction of human serum albumin with a novel antidiabetic agent–SU-118, J. Pharma. Sci. 93 (2004) 1039–1046.

[40] T. Mukherjee, M. Mukherjee, T.K. Mondal, A. Moirangthem, A. Basu, E. Zangrando, P. Chattopadhyay, Ruthenium(II) complexes of pyrrol-azo ligands: cytotoxicity, interaction with calf thymus DNA and bovine serum albumin AU - Paul, Hena, J. Coord. Chem. 66 (2013) 2747–2764.

[41] M.D. Meti, S.T. Nandibewoor, S.D. Joshi, U.A. More, S.A. Chimatadar, Multi-spectroscopic investigation of the binding interaction of fosfomycin with bovine serum albumin, J. Pharm. Anal. 5 (2015) 249–255.

[42] N. Na, D.-Q. Zhao, H. Li, N. Jiang, J.-Y. Wen, H.-Y. Liu, DNA Binding, Photonuclease activity and human serum albumin interaction of a water-soluble free-base carboxyl corrole, Molecules 21 (2015) E54 -E54.

[43] J.D.E.T. Wilton-Ely, M. Wang, S.J. Honarkhah, D.A. Tocher, Ruthenium hydride and vinyl complexes supported by nitrogen–oxygen mixed-donor ligands, Inorg. Chim. Acta. 358 (2005) 3218–3226.

[44] R.C. Maurya, A. Pandey, J. Chaurasia, H. Martin, Metal nitrosyl complexes of bioinorganic, catalytic, and environmental relevance: a novel single-step synthesis of dinitrosylmolybdenum(0) complexes of {Mo(NO)2}6 electron configuration involving Schiff bases derived from 4-acyl-3-methyl-1-phenyl-2-pyrazolin-5-one and 4-aminoantipyrine, directly from molybdate(VI) and their characterization, J. Mol. Struc. 798 (2006) 89–101.

[45] B.S. Garga, P.K. Singh, J.L. Sharma, Synthesis and characterization of transition Metal(II) complexes of salicylaldehyde-2-furoylhydrazone, Synthe. React. Inorgan. Metal-Organ. Chem. 30 (2000) 803–813.

[46] R. Karvembu, K. Natarajan, Ruthenium(III) Schiff Base Complexes: Catalytic Activity in Aryl–Aryl Coupling Reaction and Antimicrobial Activity AU - Jayabalakrishnan, C, Synthesis and Reactivity in Inorganic and Metal-Organic Chemistry, 2003, 33, 1535-1553.

[47] A. Gawin, P. Małecki, M. Dranka, J. Zachara, M. Skompska, A. Kajetanowicz, K. Grela, An unexpected formation of a Ru (III) benzylidene complex during activation of a LatMet-type ring-opening polymerisation catalyst, J. Catal. 364 (2018) 345–353.

[48] M. Aman, J. Tremmel, L. Dostál, M. Erben, J. Tydlitát, J. Jansa, R. Jambor, Highly active and selective Ru-PNH catalyst in aerobic oxidation of benzyl amines, ChemCatChem 11 (2019) 4624–4630.

[49] A. Skoczynska, M. Małecka, M. Cieslak, J. Kazmierczak-Baranska, K. Krolewska-Golinska, A. Leniart, E. Budzisz, Synthesis, structural analysis, redox properties and in vitro antitumor evaluation of half-sandwich complexes of Ru (II) with aminocoumarins, Polyhedron 127 (2017) 307–314.

[50] R. Pettinari, A. Petrini, F. Marchetti, C. Di Nicola, R. Scopelliti, T. Riedel, L.D. Pittet, A. Galindo, P.J. Dyson, Influence of functionalized η6-arene rings on ruthenium (II) curcuminoids complexes, ChemistrySelect 3 (2018) 6696–6700.

[51] A. Garza-Ortiz, P.U. Maheswari, M. Lutz, M.A. Siegler, J. Reedijk, Tuning the cytotoxic properties of new ruthenium (III) and ruthenium (II) complexes with a modified bis (arylimino) pyridine Schiff base ligand using bidentate pyridine-based ligands, J. Biol. Inorg. Chem. 19 (2014) 675–689.

[52] R.R. Kumar, R. Ramesh, J.G. Małecki, Ru (II) carbazole thiosemicarbazone complexes with four membered chelate ring: Synthesis, molecular structures and evaluation of biological activities, J. Photochem. Photobiol. B. 165 (2016) 310–327.

[53] I.P. Ejidike, P.A. Ajibade, Ruthenium (III) complexes of heterocyclic tridentate (ONN) schiff base: synthesis, characterization and its biological properties as an antiradical and antiproliferative agent, Int. J. Mol. Sci. 17 (2016) 60.

[54] R. Prabhakaran, V. Krishnan, K. Pasumpon, D. Sukanya, E. Wendel, C. Jayabalakrishnan, H. Bertagnolli, K. Natarajan, Preparation, spectral characterization, electrochemistry, EXAFS, antibacterial and catalytic activity of new ruthenium (III) complexes containing ONS donor ligands with triphenylphosphine/arsine, Appl. Organometal. Chem. 20 (2006) 203–213.

[55] N. Raja, R. Ramesh, Y. Liu, Paramagnetic ruthenium (III) complexes bearing O, O chelating ligands: synthesis, spectra, molecular structure and electron transfer properties, Polyhedron 31 (2012) 196–201.

[56] A.D. Mülazımoğlu, E. Yılmaz, İ.E. Mülazımoğlu, Dithiooxamide modified glassy carbon electrode for the studies of non-aqueous media: electrochemical behaviors of quercetin on the electrode surface, Sensors 12 (2012) 3916–3928.

[57] E. Eskelinen, P. Da Costa, M. Haukka, The synthesis and electrochemical behavior of ruthenium (III) bipyridine complexes:[Ru (dcbpy) Cl4]−(dcbpy= 4, 4′-dicarboxylic acid-2, 2′-bipyridine) and [Ru (bpy) Cl3L](L= CH3OH, PPh3, 4, 4′-bpy, CH3CN), J. Electroanal. Chem. 579 (2005) 257–265.

[58] F. Basuli, A.K. Das, G. Mostafa, S.-M. Peng, S. Bhattacharya, Chemistry of ruthenium with some phenolic ligands: synthesis, structure and redox properties, Polyhedron 19 (2000) 1663–1672.

[59] R. Ramesh, K. Natarajan, Synthesis and spectral studies of ruthenium (III) complexes with (mono, di-seleno) bis (β-diketone) and imidodi (thiocarbonic acid-O-alkyl ester), Ind. J. Chem. 34 (1995) 535–539.

[60] I.N. Booysen, S. Maikoo, M.P. Akerman, B. Xulu, Isolation of ruthenium compounds with bidentate benz(imidazole/othiazole) chelators, Trans. Met. Chem. 40 (2015) 397–404.

[61] M. Loza, A.Z. Slawin, Complexes of ruthenium with tridentate [P, N, O] ligands, J. Chem. Soc., Dalton Trans. (1999) 2917–2921.

[62] P. Govindaswamy, M.R. Kollipara, Syntheses of (η6-p-cymene) ruthenium (II) piano-stool amine complexes: molecular structure of [(η6-C10H14) RuCl2 (H2N-C6H4-p-Cl)], J. Coord. Chem. 59 (2006) 131–136.

[63] J.-m. Manoli, A.P.Gaughan Jr, J.A. Ibers, The structure of dichlorobis (phenylamine)(bicyclo [2.2. 1] hepta-2, 5-diene) ruthenium: a π-bonded norbornadiene complex of ruthenium (II), J. Organomet. Chem. 72 (1974) 247–259.

[64] L.R. Dinelli, G. Von Poelhsitz, E.E. Castellano, J. Ellena, S.E. Galembeck, A.A. Batista, On an electrode modified by a supramolecular ruthenium mixed valence (RuII/RuIII) diphosphine-porphyrin assembly, Inorg. Chem. 48 (2009) 4692–4700.

[65] S.Q. Wu, Y. Miyazaki, M. Nakano, S.Q. Su, Z.S. Yao, H.Z. Kou, O. Sato, Slow magnetic relaxation in a mononuclear ruthenium (III) complex, Chemistry–A European Journal 23 (2017) 10028–10033.

[66] P. Braunstein, D. Matt, D. Nobel, S.-E. Bouaoud, B. Carluer, D. Grandjean, P. Lemoine, Complexes with functional phosphines. Part 8. Interconversion study of [RuCl 2 {Ph 2 PCH 2 C (O) OEt} L 2],[RuCl 2 (CO){Ph 2 PCH 2 C (O) OEt} L], and [RuCl 2 (CO) 2 L 2][L= Ph 2 PCH 2 C (O) OEt] under CO. Synthesis and X-ray structure of mer-[RuCl 3 {Ph 2 PCH 2 C (O) OEt} L], J. Chem. Soc., Dalton Trans. (1986) 415–419.

[67] J.V. McArdle, A.J. Schultz, B.J. Corden, R. Eisenberg, Coordination of the arylazo group. Molecular structure of trichloro (p-tolylazo) bis (tiphenylphosphine) ruthenium (II)-acetone, RuCl3 (p-N2C6H4Me)(PPh3) 2. Me2CO, Inorg. Chem. 12 (1973) 1676–1681.

[68] W.J. Hehre, in: A Guide to Molecular Mechanisms and Quantum Chemical Calculations, Wavefunction Inc., Irvine, CA, USA, 2003, pp. 153–181.

[69] G.-J. Cao, X. Jiang, H. Zhang, J. Zheng, T.R. Croley, J.-J. Yin, Exploring the activities of ruthenium nanomaterials as reactive oxygen species scavengers, J. Environ. Sci. Health 35 (2017) 223–238 Part C.

[70] T.S. Kamatchi, P. Kalaivani, F.R. Fronczek, K. Natarajan, R. Prabhakaran, Impact of chelation on anticancer activities of organometallic ruthenium (ii) complexes containing 2, 5-di (1 H-pyrazol-1-yl)-1, 4-benzoquinone: synthesis, structure, DNA/protein binding, antioxidant activity and cytotoxicity, RSC Adv 6 (2016) 46531–46547.

[71] M. Mohanraj, G. Ayyannan, G. Raja, C. Jayabalakrishnan, Ruthenium (II) complexes containing 4-methoxybenzhydrazone ligands: synthesis, characterization, DNA binding, DNA cleavage, radical scavenging and in vitro cytotoxic activity, Appl. Organometal. Chem. 30 (2016) 550–560.

[72] M. Mohanraj, G. Ayyannan, G. Raja, C. Jayabalakrishnan, Synthesis, spectral characterization, DNA interaction, radical scavenging and cytotoxicity studies of ruthenium (II) hydrazone complexes, J. Photochem. Photobiol. B. 158 (2016) 164–173.

[73] P. Jayaseelan, S. Prasad, S. Vedanayaki, R. Rajavel, Synthesis, characterization, anti-microbial, DNA binding and cleavage studies of Schiff base metal complexes, Arab. J. Chem. 9 (2016) S668–S677.

[74] T.S. Kamatchi, N. Chitrapriya, H. Lee, C.F. Fronczek, F.R. Fronczek, K. Natarajan, Ruthenium (II)/(III) complexes of 4-hydroxy-pyridine-2, 6-dicarboxylic acid with PPh3/AsPh3 as co-ligand: impact of oxidation state and co-ligands on anticancer activity in vitro, Dalton Trans 41 (2012) 2066–2077.

[75] A.P. Carnizello, M.I. Barbosa, M. Martins, N.H. Ferreira, P.F. Oliveira, G.M. Magalhães, A.A. Batista, D.C. Tavares, In vitro and in vivo antitumor activity of a novel carbonyl ruthenium compound, the ct-[RuCl (CO)(dppb)(bipy)] PF6 [dppb= 1, 4-bis (diphenylphosphine) butane and bipy= 2, 2′-bipyridine], J. Inorg. Biochem. 164 (2016) 42–48.

[76] F.A. Beckford, A. Stott, P.C. Mbarushimana, M.-A. LeBlanc, K. Hall, S. Smith, J.L. Bullock, D.J. Houghton, A.A. Holder, N. Gerasimchuk, Anticancer, biophysical and computational investigations of half-sandwich ruthenium (II) thiosemicarbazone complexes: The effect of arene versus thiacrown face-cap, Interdiscip. J. Chem. 1 (2016) 1–15.

[77] S. Sathiyaraj, K. Sampath, C. Jayabalakrishnan, Synthesis, Spectral Characterization, DNA Binding, DNA Cleavage, and Antioxidant Studies of Ruthenium (III) Heterocyclic Thiosemicarbazone Complexes, Synthesis and Reactivity in Inorganic, Metal-Organic, and Nano-Metal Chemistry, 2014, 44, 1261-1271.

[78] N. Shahabadi, S.Moradi Fili, DNA-interaction studies of a copper (II) complex containing ceftobiprole drug using molecular modeling and multispectroscopic methods, J. Coord. Chem. 71 (2018) 2843–2855.

[79] G. Raja, C. Jayabalakrishnan, Organoruthenium (II) thiosemicarbazone complexes: synthesis, spectral characterization, DNA binding and DNA cleavage studies, Cent, Eur. J. Chem. (11) (2013) 1010–1018.

[80] W.M. Motswainyana, P.A. Ajibade, Anticancer activities of mononuclear ruthenium (II) coordination complexes, Adv. Chem. 2015 (2015) 1–21.

[81] P. Zhang, J. Chen, Y. Liang, DNA binding, cytotoxicity, and apoptotic-inducing activity of ruthenium (II) polypyridyl complex, Acta. Biochim. Biophys. Sin. 42 (2010) 440–449.

[82] M.N. Patel, H.N. Joshi, C.R. Patel, DNA binding Cytotoxic, DNA cleavage and antibacterial studies of ruthenium–fluoroquinolone complexes, J. Chem. Sci. 126 (2014) 739–749.

[83] J.a. Zhao, S. Zhi, H. Yu, J. Zhang, J. Zhang, J. Hu, Synthesis, crystal structure, DNA/BSA interaction and in vitro antitumor activity of N-heterocycle Cu (II) and Co (II) complexes, J. Coord. Chem. 70 (2017) 3110–3131.

[84] Q. Zhang, Y. Ni, Comparative studies on the interaction of nitrofuran antibiotics with bovine serum albumin, RSC Adv. 7 (2017) 39833–39841.

[85] X. Lei, L. Ya-nan, M. Wen-jie, H. Xiao-mei, C. Tian-feng, L. Jie, Z. Wen-jie, Interaction of Mixed Porphyrin-polypyridyl Ru (II) Complex with Bovine Serum Albumin, Chem. Res. Chinese Universities 26 (2010) 693–698.

[86] Z. Chi, B. Hong, X. Ren, K. Cheng, Y. Lu, X. Liu, Investigation on the conformational changes of bovine serum albumin in a wide pH range from 2 to 12, Spectroscopy Letters 51 (2018) 279–286.

[87] R. Kumaran, P. Ramamurthy, Denaturation mechanism of BSA by urea derivatives: evidence for hydrogen-bonding mode from fluorescence tools, J. Fluoresc. 21 (2011) 1499–1508.
[88] M. Rajabi, M.A. Khalilzadeh, F. Tavakolinia, P. Signorelli, R. Ghidoni, E. Santaniello, Naphthalene-fused (α-alkoxycarbonyl) methylene-γ-butyrolactones: antiproliferative activity and binding to bovine serum albumin and DNA, DNA Cell Biol. 31 (2012) 783–789.
[89] V.D. Suryawanshi, L.S. Walekar, A.H. Gore, P.V. Anbhule, G.B. Kolekar, Spectroscopic analysis on the binding interaction of biologically active pyrimidine derivative with bovine serum albumin, J. Pharm. Anal. 6 (2016) 56–63.
[90] A.-Z. Wu, C.-Z. Lin, Y.-J. Zhai, J.-L. Zhuo, C.-C. Zhu, Investigation of the interaction between two phenylethanoid glycosides and bovine serum albumin by spectroscopic methods, J. Pharm. Anal. 3 (2013) 61–65.
[91] T. Topală, A. Bodoki, L. Oprean, R. Oprean, Bovine serum albumin interactions with metal complexes, Clujul Med. 87 (2014) 215–219.
[92] A.C. de Melo, J.M. Santana, K.J. Nunes, B.L. Rodrigues, N. Castilho, P. Gabriel, A.H. Moraes, M.d.A. Marques, G.A. de Oliveira, Í.P.de Souza, New heteroleptic ruthenium (II) complexes with sulfamethoxypyridazine and diimines as potential antitumor agents, Molecules 24 (2019) 2154.
[93] V. Ravi Kumar, P. Nagababu, G. Srinivas, M. Rajender Reddy, M. Vinoda Rani, M. Ravi, S. Satyanarayana, Investigation of DNA/BSA binding of three Ru (II) complexes by various spectroscopic methods, molecular docking and their antimicrobial activity, J. Coord. Chem. 70 (2017) 3790–3809.
[94] A. Varlan, M. Hillebrand, Bovine and human serum albumin interactions with 3-carboxyphenoxathiin studied by fluorescence and circular dichroism spectroscopy, Molecules 15 (2010) 3905–3919.
[95] B. Ojha, G. Das, Role of hydrophobic and polar interactions for BSA–amphiphile composites, Chem. Phys. Lipids 164 (2011) 144–150.
[96] X. Zhang, L. Li, Z. Xu, Z. Liang, J. Su, J. Huang, B. Li, Investigation of the interaction of naringin palmitate with bovine serum albumin: spectroscopic analysis and molecular docking, PLoS One 8 (2013) e59106.
[97] F. Zsila, Subdomain IB is the third major drug binding region of human serum albumin: toward the three-sites model, Mol. pharmaceutics 10 (2013) 1668–1682.
[98] I.N. Booysen, A. Adebisi, M.P. Akerman, Formation, electrochemical and radical scavenging properties of novel ruthenium compounds with N, X-donor (X= O, N) heterocyclic chelators, Inorg. Chim. Acta. 433 (2015) 13–20.
[99] S. Son, B.A. Lewis, Free radical scavenging and antioxidative activity of caffeic acid amide and ester analogues: Structure− activity relationship, J. Agric. Food Chem. 50 (2002) 468–472.
[100] E. Bendary, R. Francis, H. Ali, M. Sarwat, S. El Hady, Antioxidant and structure–activity relationships (SARs) of some phenolic and anilines compounds, Ann. Agric. Sci. 58 (2013) 173–181.
[101] V. Suryanti, F. Wibowo, S. Khotijah, N. Andalucki, Antioxidant activities of cinnamaldehyde derivatives, IOP Confe. Series 333 (2018) 012077.
[102] M. Abbdellaoui, E.d.T. Bouhlali, L.E. Rhaffari, Chemical composition and antioxidant activities of the essential oils of cumin (cuminum cyminum) conducted under organic production conditions, J. Essent. Oil-Bear. Plants. 22 (2019) 1500–1508.
[103] E. Csepanyi, P. Szabados-Furjesi, A. Kiss-Szikszai, L.M. Frensemeier, U. Karst, I. Lekli, D.D. Haines, A. Tosaki, I. Bak, Antioxidant properties and oxidative transformation of different chromone derivatives, Molecules 22 (2017) 588.
[104] R. Teran, R. Guevara, J. Mora, L. Dobronski, O. Barreiro-Costa, T. Beske, J. Pérez-Barrera, R. Araya-Maturana, P. Rojas-Silva, A. Poveda, Characterization of antimicrobial, antioxidant, and leishmanicidal activities of Schiff base derivatives of 4-aminoantipyrine, Molecules 24 (2019) 2696.
[105] P. Zhao, S. Zhai, J. Dong, L. Gao, X. Liu, L. Wang, J. Kong, L. Li, Synthesis, structure, DNA interaction, and SOD activity of three nickel (II) complexes containing L-phenylalanine Schiff base and 1, 10-phenanthroline, Bioinog. Chem. Appl. (2018) 2018.
[106] W. Xi, F.-Q. Song, X.-L. Xia, X.-Q. Song, Tuned structure and DNA binding properties of metal complexes based on a new 4-acylpyrazolone derivative, New. J. Chem. 44 (2020) 2281–2290.
[107] L. Messori, P. Orioli, D. Vullo, E. Alessio, E. Iengo, A spectroscopic study of the reaction of NAMI, a novel ruthenium(III)anti-neoplastic complex, with bovine serum albumin, Eur J Biochem 267 (2000) 1206–1213.
[108] T.T. Herskovits, B. Gadegbeku, H. Jaillet, On the structural stability and solvent denaturation of proteins: I. Denaturation by the alcohols and glycols, J. Biol. Chem. 245 (1970) 2588–2598.
[109] A. Mishra, A. Malakar, H.T. Biswal, M.K. Barman, G. Krishnamoorthy, Interactions of a few azole derivatives with a transport protein: role of heteroatoms, J. Mol. Recognit. 28 (2015) 299–305.